Verification of Numerical Models for Hydrothermal Plume Water through Field Measurements at TAG

by

Sacha Wichers

Submitted to the Joint Program in Applied Ocean Science and Engineering in partial fulfillment of the requirements for the degree of

Master of Science in Ocean Engineering

at the

MASSACHUSETTS INSTITUTE OF TECHNOLOGY

and the

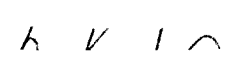WOODS HOLE OCEANOGRAPHIC INSTITUTION

February 2005
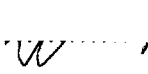
Author.....
....
Joint Program in Applied Ocean Science and Engineering
January 12th 2005

Certified by..
....
Hanumant Singh
Associate Scientist, WHOI
Thesis Supervisor

Certified by...........
....
Rob Reves-Sohn
Associate Scientist, WHOI

Accepted by..........
....
Mark Grosenbaugh
Associate Scientist, WHOI
Chairman, Joint Committee for Applied Ocean Science and Engineering
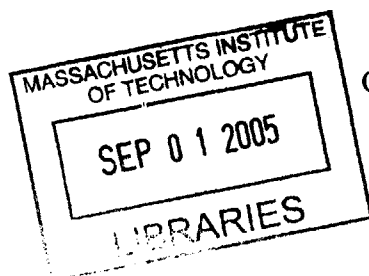
BARKER

Verification of Numerical Models for Hydrothermal Plume Water through Field Measurements at TAG

by

Sacha Wichers

Submitted to the Joint Program in Applied Ocean Science and Engineering in partial
fulfillment of the requirements for the degree of
Master of Science in Ocean Engineering

Abstract

Hydrothermal vents discharge superheated, mineral rich water into our oceans, thereby providing a habitat for exotic chemosynthetic biological communities. Hydrothermal fluids are convected upwards until they cool and reach density equilibrium, at which point they advect laterally with the current. The neutrally buoyant plume layer can have length scales on the order of several kilometers, and it therefore provides the best means to detect the presence of vent fields on the seafloor, which typically have length scales on the order of a few meters. This thesis uses field measurements of the velocity, temperature and particulate anomalies associated with the TAG hydrothermal plume to demonstrate that tidal currents exert a strong impact on the plume shape, and to provide new constraints on the thermal power of the TAG hydrothermal system. The results show that the power output of the TAG system is on the order of 6000 MW, which is up to two orders of magnitude greater than previous estimates, and that there is considerably more entrainment than had previously been assumed.

Thesis Supervisor: Hanumant Singh
Title: Associate Scientist, WHOI

Thesis Supervisor: Rob Reves Sohn
Title: Associate Scientist, WHOI

Thesis Supervisor: Gene Terray
Title: Research specialist, WHOI

ACKNOWLEDGEMENTS

Thanks to:

CONTENTS

Section 4: Modeling the neutrally buoyant layer of the plume

LIST OF FIGURES

SECTION 1: INTRODUCTION

1.1 Scientific objectives at hydrothermal vents

Hydrothermal vent fields are typically located at the boundary between diverging tectonic plates, the so-called spreading centers or mid ocean ridges (MORs). Figure 1 shows the MORs– bathymetric features that rise above the abyssal plains in the ocean basins, and the location of the hydrothermal vent field TAG.
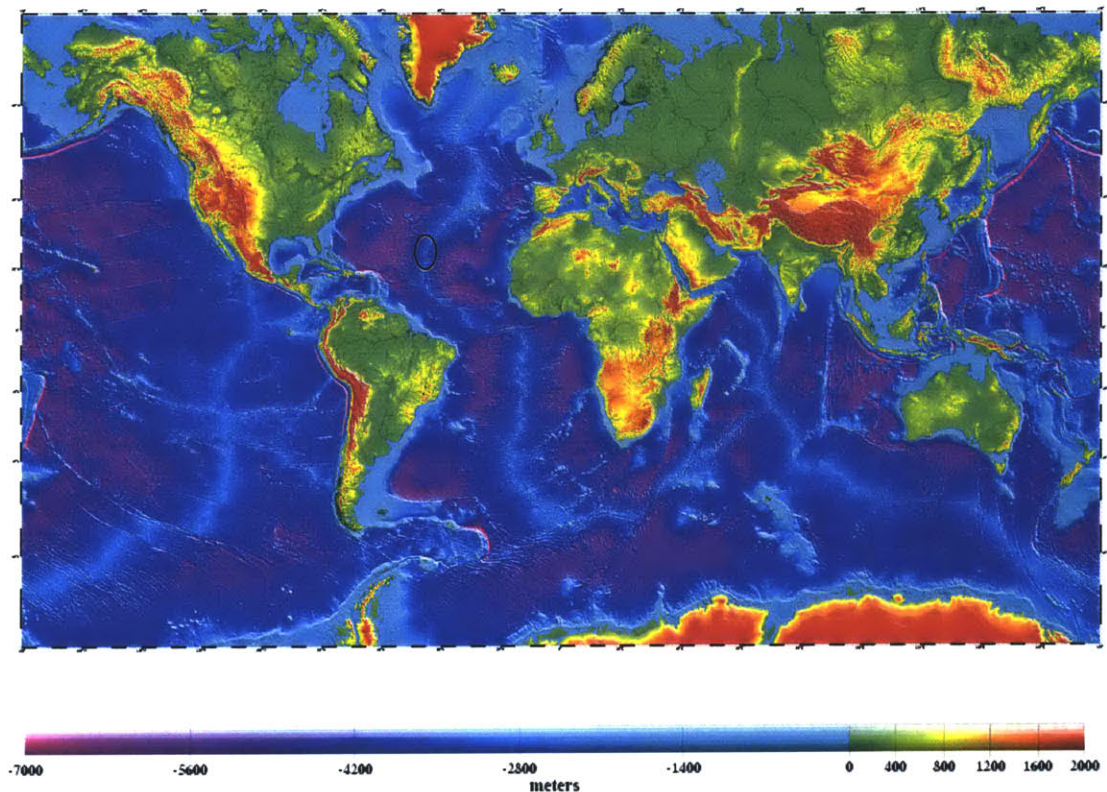
Figure 1: Global topographic relief map with the location of TAG shown by the black circle. (Courtesy of C. Small, Lamont Doherty Earth Observatory.)

Hydrothermal vents were first discovered in the 1970s, (Hannington 1999) and have captured intense scientific interest ever since. Indications of hydrothermal activity at TAG were first found in 1972,when Peter Rona found excess sulfide when he was part of the 1972 Trans Atlantic Geo Traverse expedition. (Peter Rona, personal comm. July 2003)

Life flourishes near hydrothermal vents because bacteria use reduced ions, mainly sulfide S^{2-}, that are present in hydrothermal plume water to convert inorganic matter to organic substance in a process called chemosynthesis. The bacteria then form the basis of an ecosystem that exists without the aid of photosynthesis (Hessler 1995).

Hydrothermal vents are driven by inner earth processes, and may tell us both what is going on inside our planet, as well as play a roll in our climate by transferring heat from the lithosphere into the ocean. Scientists have found that there is a greater net loss of heat than gain from the ocean, and perhaps the hydrothermal vents account for this difference. (Pickard 1990). Hydrothermal vents may also contribute to the balance of the chemical composition of seawater. Magnesium for example leaches into the ocean from the land, yet there is no net increase of magnesium. It is now known that magnesium rich seawater descending into the earth's crust loses all its magnesium by the time the seawater exits the seafloor. Many other elements (most notably lithium, potassium, rubidium, cesium, manganese, iron, zinc, and copper) find their way into seawater through hydrothermal venting. (Tivey 2004)

1.2 Physics of hydrothermal circulation

Wherever two tectonic plates diverge new rock is formed as hot matter rises up to fill the void created by the spreading plates. This rock is very porous, so water may seep through this young rock to depths between 1 and 2 kilometers. (Alt 1995) If there is a source of heat (a magma chamber for example), the water will get very hot and, because of its density deficit, convect up out of the seafloor and into the water column through well-established conduits. The hot fluid will rise much like smoke from a smokestack,

entraining ambient seawater until its density is equal to the ambient density. During the descent of the seawater through the so-called recharge zone the seawater experiences a decrease in pH, and a loss of oxygen. Close to the heat source, in the so-called reaction zone, the water reduces further, and this hot reducing acidic water dissolves the metals present in the rock. Once all the oxygen in the seawater is used up SO_4^{2-} turns into H_2S. This hydrogen sulfide is the main compound that forms the chimney. Upon reentry of the fluids into the water column the metals precipitate out as metal sulfides, from which the water gets its characteristic black color. The black smokers are dramatic features on the ocean floor, but there is also secondary or diffuse venting near these smokers. The porosity of the young rock allows water to circulate through it and, much like a heat exchanger, this circulating water is heated by the hot hydrothermal plume water. Figure 2 shows one of the larger chimneys of TAG. Note the shrimp that cluster around its base.

Figure 2: Major chimney on TAG

1.3 Thesis Outline

This thesis focuses on modeling the extent of the plume water after it leaves the chimney. The water initially is convected upwards, and I used models developed by G.I. Taylor (Morton 1956), and described by Turner (Turner 1973), to predict both heat flux and rise height of the plume given the initial conditions of exhaust area and velocity at the seafloor. The ambient water mixes with the turbulent plume until there no longer is a density deficit. The plume water can still be detected because heat is conserved, and a detectable temperature anomaly may be observed. This plume water is advected by the local currents. I used a model developed by Wetzler and Lavelle (Lavelle 1998) to predict the extent of the advected plume water. Both the convective and the advective model use conservation equations, and as heat is conserved it makes temperature the tracer of choice. Not all conservative tracers are useful for plume finding and mapping; 3He for example is only lost to the atmosphere, and while it is an indicator of hydrothermal venting, 3He can be found thousands of kilometers from its origin. The ratio of conservative to non-conservative tracers has been used to determine the age of the plume, (Kadko 1990) particularly the radon/3He ratio. Klinkhammer has used manganese as a plume tracer (Klinkhammer 1986). Metals are generally not conserved, and detection in situ proves difficult to this present day. The collected data at TAG, presented in this thesis, includes measurements with two different CTD packages, a transmissometer, an optical backscatterer, and a 300 kHz ADCP. The measurements at TAG show that the outer edge of the detectable temperature anomaly corresponds nicely with the maximum observed decrease in turbidity of the water, resulting in a consistent rendering of the plume. For a further discussion on plume detection the reader is referred to articles by Lupton, McDuff and Baker in Seafloor Hydrothermal Systems. (Humphris et all, 1995)

SECTION 2: FIELD MEASUREMENTS

2.1: Instrument specification

We collected field data of the TAG plume during two expeditions, STAG I (6-7/2003) and STAG IV (10-11/2004). We used Atlantis' CTD package to collect 27 hours worth of CTD data during the nights of 6/30–7/2 in the neutrally buoyant layer (NBL) of the plume during STAG I, and we used the ROV Jason to collect 24 hours of CTD data on 11/03 in the NBL during STAG IV. During STAG I Alvin was used during the day to take various vent measurements, and at night Atlantis II towed the rosette without bottles, but with the Seabird 911 plus CTD package. This standard WHOI CTD package includes Wetlabs C-Star 660 nm wavelength, 25 cm path length transmissometer, with a response time of .167 seconds. Table 1 gives the specifications of the CTD sensors:

	Temperature (°C)	Conductivity (S/m)	Pressure
Measurement Range	-5 to +35	0 to 7	0 to full scale range (in meters of deployment depth capability): 1400 / 2000 / 4200 / 6800 / 10500 meters
Initial Accuracy	0.001	0.0003	0.1% of full scale range
Typical Stability/Month	0.0002	0.0003	0.0015% of full scale range
Resolution at 24 Hz	0.0002	0.00004	0.001% of full scale range
Sensor Calibration (measurement outside these ranges may be at slightly reduced accuracy due to extrapolation errors)	-1.4 to +32.5	2.8 to 6.1 S/m. plus zero conductivity (air)	Paroscientific calibration. plus Sea-Bird temperature correction
Time Response (single pole approximation including sensor and acquisition system contributions)	0.065 seconds	0.065 seconds	0.015 seconds

Table 1: Instrument specification.

During STAG IV we used a Seabird Fastcat CTD, and Wetlab's optical scattering meter, the ECO-BBTD. Both were mounted on ROV Jason. We also deployed an ADCP on the seafloor in the axial valley. We were able to get CTD and optical backscatter data in real time in both cases. In order to cover as much spatial content as possible, and get a synoptic picture of the plume we settled on sampling the water moving the sensor package up and down in a so-called tow-yo pattern. During STAG I Atlantis' speed was limited by the tension in the winch cable and moved at slightly less than 0.5 knots. The average vertical excursion was 450 meters, during which we proceeded 250 meters. This translates in an average speed of about 0.68 m/s through the water for the CTD package.

During STAG IV Jason moved through the water at about .5 m/s and was therefore able to cover approximately the same distance per time period. We aligned our survey with the axial valley, assuming that tidal flow, and therefore the shape of the neutrally buoyant layer, will be oriented along the axial valley. This assumption proved a good one, and so we aligned our track with the axial valley in 2004 as well. For the 2003 cruise the data is plotted vs the ship track. Since the rosette trailed the ship by anywhere from 0 to 700 meters we will use the data from the 2004 cruise to show in figure 2 where hydrothermal plume water was found. During the 2004 cruise we were able to get very accurate LBL nav from the Jason transponder network. Figure 3 shows the bathymetry near the TAG hydrothermal vent field. The cross marks the location of TAG: 44°49'W, 26°08' N at a depth of 3650 meters. The diamond shows where we deployed the ADCP in the 2004 cruise.

2.2 Bathymetry and seawater properties at TAG

Bathymetry of the TAG mound
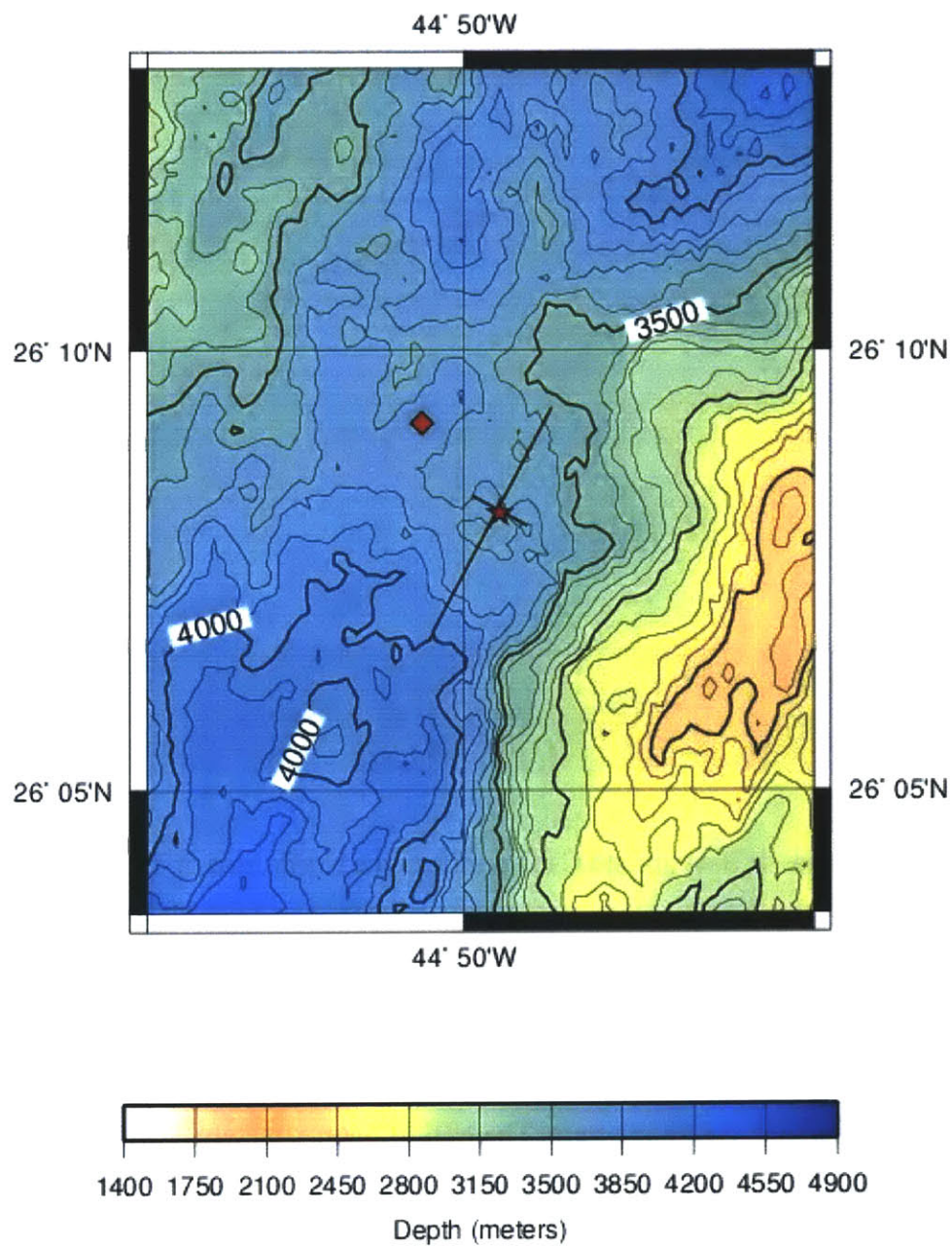
Figure 3: Tag site and track showing hydrothermal fluid.

Figure 4 shows a typical Atlantic CTD profile taken 2 km NW of the TAG vent field. The salinity decreases with depth in the Atlantic Ocean as opposed to the Pacific Ocean where the salinity increases with depth.
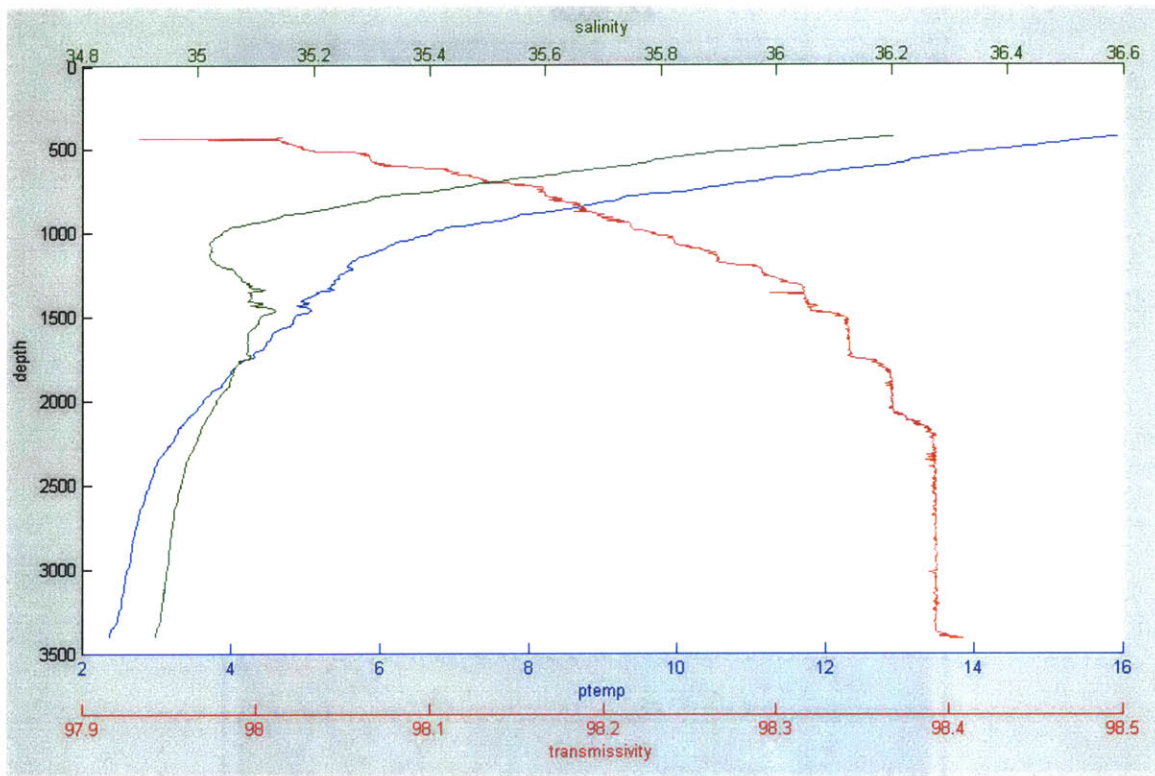
Figure 4: Background CTD profile taken North-East of TAG.

Both figures 4 and 5 were made using data from the 2003 cruise. Figure 5 shows the CTD profile taken on top of the TAG mound. The spike around 3375 meters depth perhaps signifies the bottom of the NBL of the plume. The intense signal below 3550 meters is attributable to the plume stem. The NBL is approximately 225 meters thick, roughly between 3150 and 3375 meters depth. The bathymetry around TAG is treacherous – steep outcrops with vertical reliefs of at least 100 meters are ubiquitous – but the main sulfide complex lays at a depth of 3650 meters. The NBL then is between

275 and 500 meters off the bottom. The NBL remains remarkably well confined at this depth. When we returned a year later we found the plume at approximately the same depth.

Since the vent field lays at a depth of 3650 meters the compressibility effects of water must be taken into account. Temperature and density are converted into potential temperatures and densities; the potential temperature is the temperature the water would have had if it were raised adiabatically to the surface (Pickard1964).
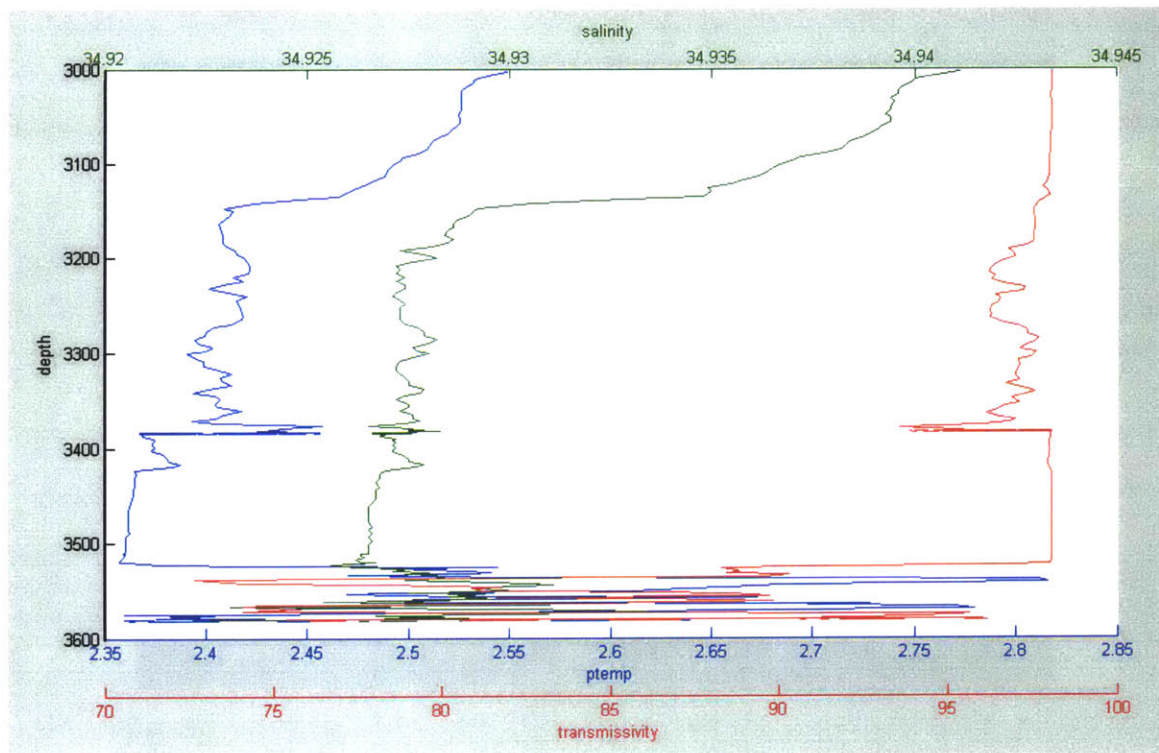
Figure 5: CTD profile above the TAG mound.

The transmissivity data shown in figures 4 and 5 demonstrate that the hot exit vent fluid contains a lot of particulate matter, whereas the rest of the seawater has a constant turbidity. In ambient ocean water the percentage of light that reaches the transmissometer's receiver is 98.4. In the neutrally buoyant part of the plume the light received drops to 95%. This large anomaly makes the transmissometer an instrument that is well suited to plume detection work. The temperature anomalies are much more subtle,

typically on the order of hundreds of a degree. The temperature anomaly from the background does not give a clear signal of the plume. However, the deviation of the potential temperature from the background temperature salinity plot is coherent. (Lupton, 1995) The red dots in figure 6 show the relationship between temperature and salinity 2 km away from the TAG mound, while the blue dots show that the background T-S plot is linear in the absence of plume activity. The temperature anomaly is calculated as the difference between the temperature predicted by the linear T-S relationship and the actual temperature.
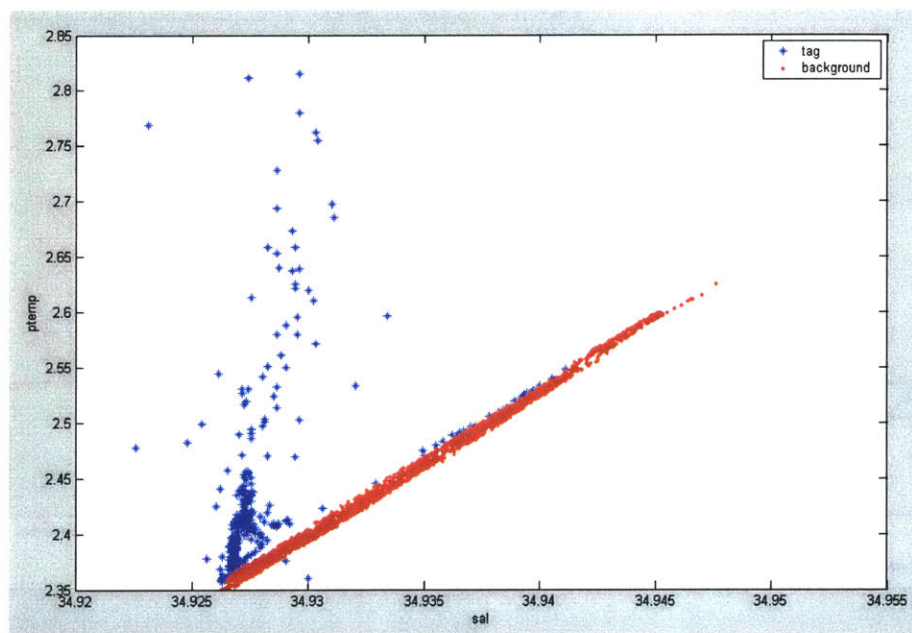
Figure 6: T-S plot on TAG and 2 km away from any plume activity.

As the plume rises it entrains ambient water to overcome its density deficit. When the plume has entrained enough cold water to overcome its temperature deficit it has entrained the fresher, lighter bottom water and must rise yet higher to attain neutral buoyancy. As a result, the NBL of an Atlantic plume is colder and fresher than the ambient water at the same depth (Speer et all, 1989). This is evident from the following plot, where along the isopycnal surfaces (indicating constant depth) the temperature of TAG plume water is lower than the ambient temperature.
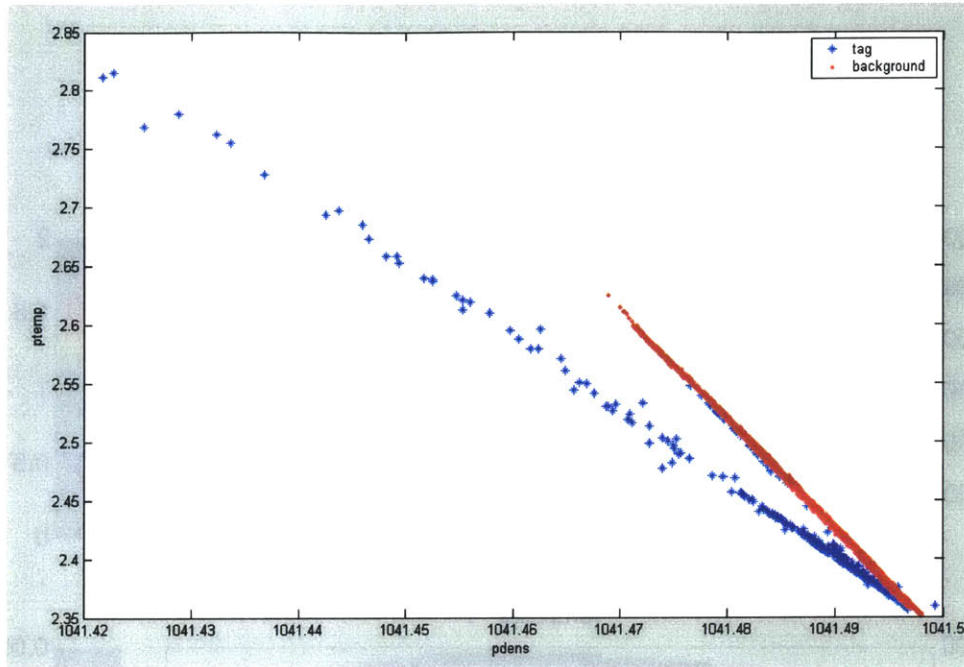
Figure 7: Potential density vs potential temperature.

2.3: Spatial extent of the TAG plume

Figures 8-10 show the temperature and transmissivity anomalies in the NBL measured during STAG I. We took samples three consecutive nights at the same time during a tidal cycle for periods of no more than three hours. Assuming currents at TAG have tidal periods, three hours could be viewed as a time averaged stationary view of the plume.

Figure 8 shows the track starting on the TAG mound heading west perpendicular to the direction of the axial valley. The x-axis is the distance from the TAG mound in meters. The y-axis is the depth. The color of the plot gives the strength of the anomaly. Note that the x-axis gives the ship track, not the rosette track. As the rosette trails the ship by up to 700 meters we may assume that the half width of the plume on the cross axial track shown in figure 8 was no more then 900 meters.
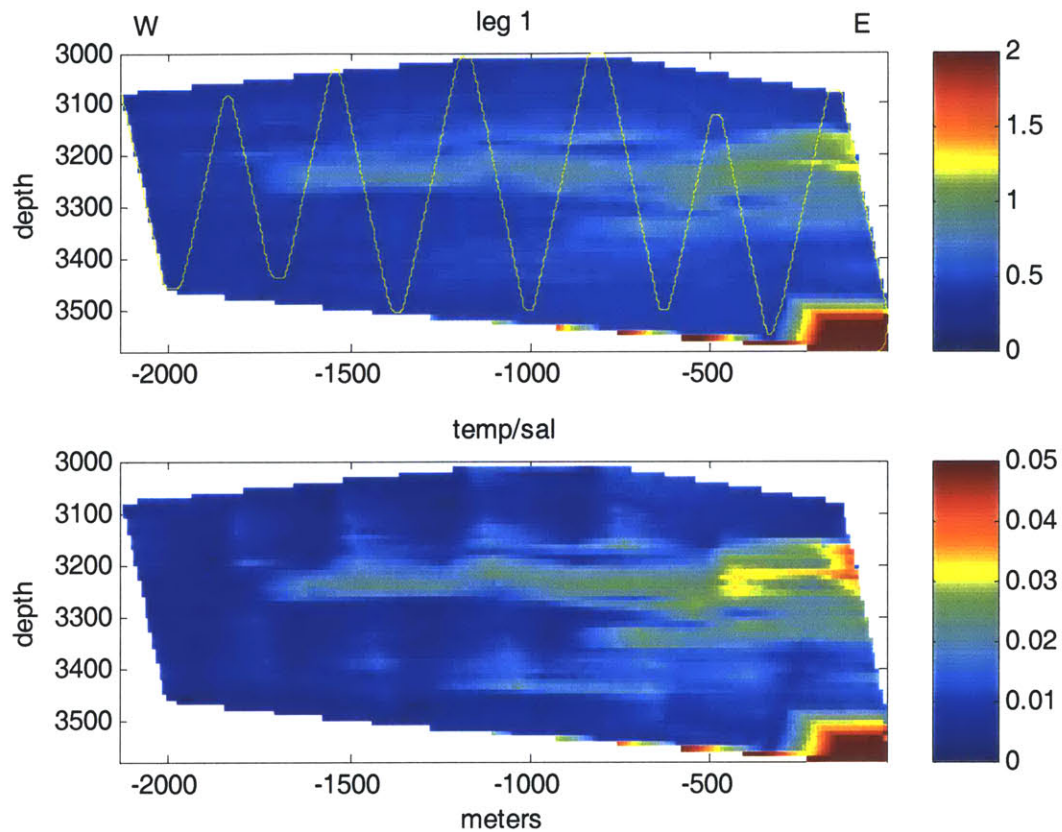
Figure 8: Plume activity on the cross axial leg (2003).

The top plot in figure 8 shows the transmissivity anomaly, and the bottom plot shows the temperature deviation from the T-S plot. Figures 8, 9, and 10 are drawn to the same scale to enable direct comparison of the relative strengths of the anomalies. The transmissivity plot has the actual tow-yow track lines superimposed on it. The two plots show a high degree of correlation. The temperature plot shows slightly warmer temperatures along the upcasts of the tow-yow path, likely an artifact of CTD operation. Figure 9 shows the results from the survey track starting south of the mound, and proceeding along the axial valley towards and over the TAG complex.
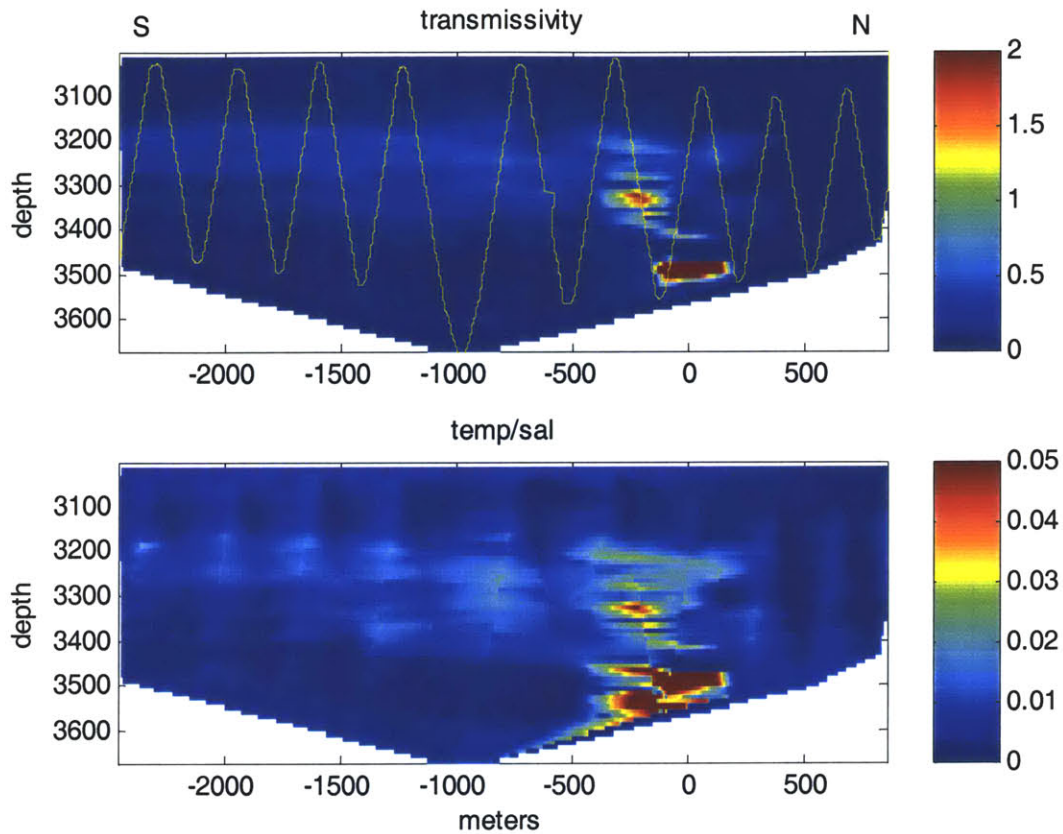
Figure 9: Transmissivity and temperature anomalies S-W of TAG (2003).

Again the x-axis represents the distance from the mound as traveled by the ship, and the y-axis gives the depth of the rosette. We encountered plume activity as far as 2 kilometers S-W of the mound, but once we passed over the mound the plume activity stopped. The bottom currents appear to force the plume to bend over as shown in the figure 9. The buoyant part of the plume can also be seen in this figure; the stem is hotter and more particulate laden than the neutrally buoyant part of the plume.

The last survey track containing a plume signal is shown in figure 10. This track is perpendicular to the axial valley, roughly 300 meters south of the mound.

Figure 10: Cross axial track (2003).

The above plot has nicely correlated temperature and particulate anomalies. However, there is a feature to the southeast, or to the right of the origin in the above plot, that is seen in temperature, but not particulate anomaly. It is possible that this is warm water, heated by diffusion, without much particle anomalies.

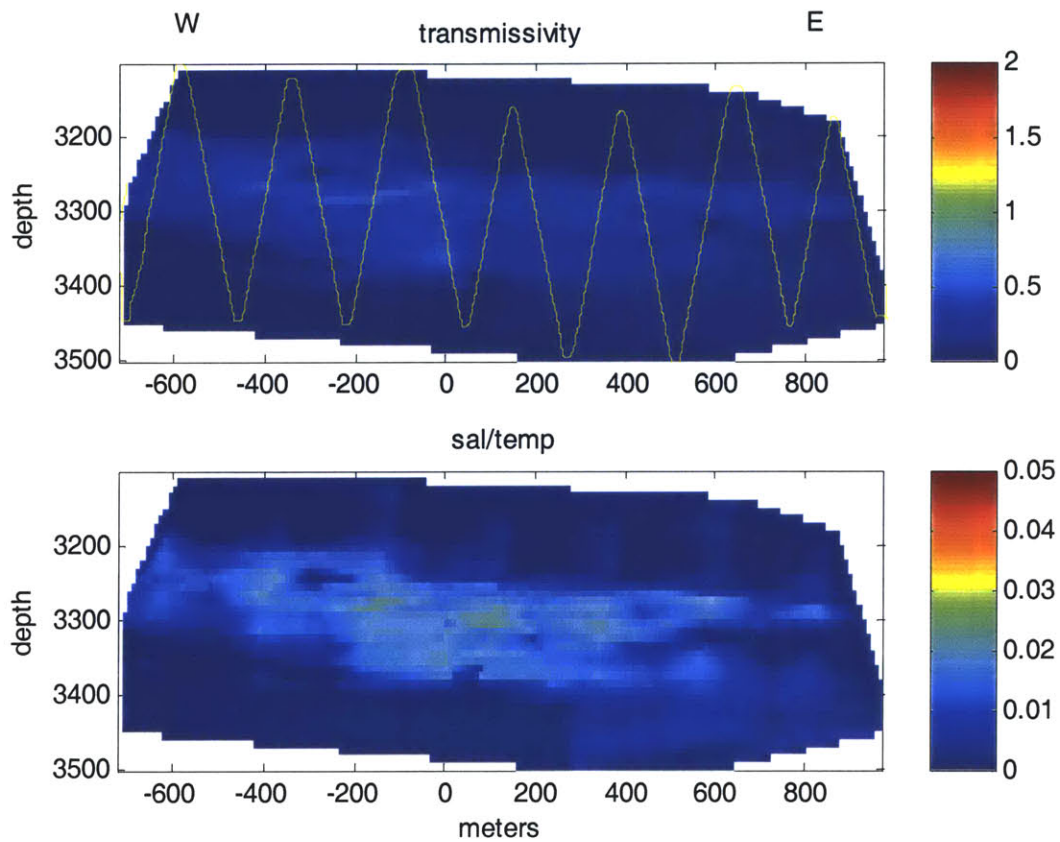During STAG IV we had a 24 hour window on November 3rd 2004 to make more measurements of the neutrally buoyant plume. We again opted for the tow-yo pattern as that appears the most efficient way to sample the plume.

Again visualization of the plume water was achieved through looking at the temperature anomaly from the T-S plot. We started at the TAG mound and moved away to the south along the axial valley (figure 11) until we did not observe any more plume activity. We then reversed our course and continued north along the axial valley until we reached the northern most limit of the plume (figure 12). We then reversed course once more and continued south along the axial valley until we arrived at the TAG mound again (figure 13).
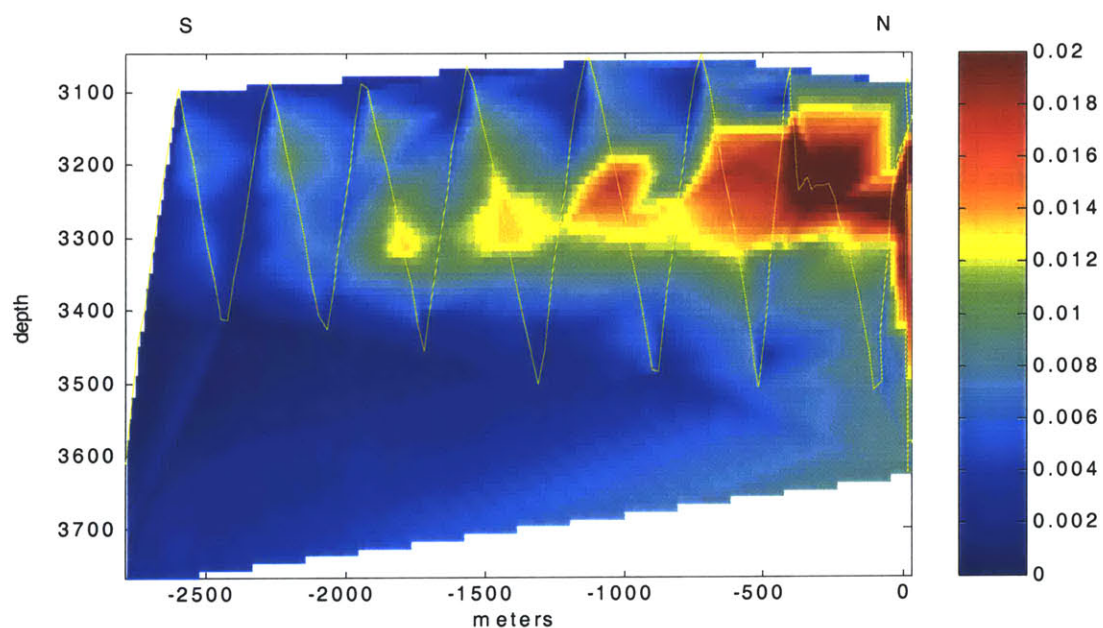

Figure 11: Temperature anomaly as proxy for hydrothermal plume water (2004).
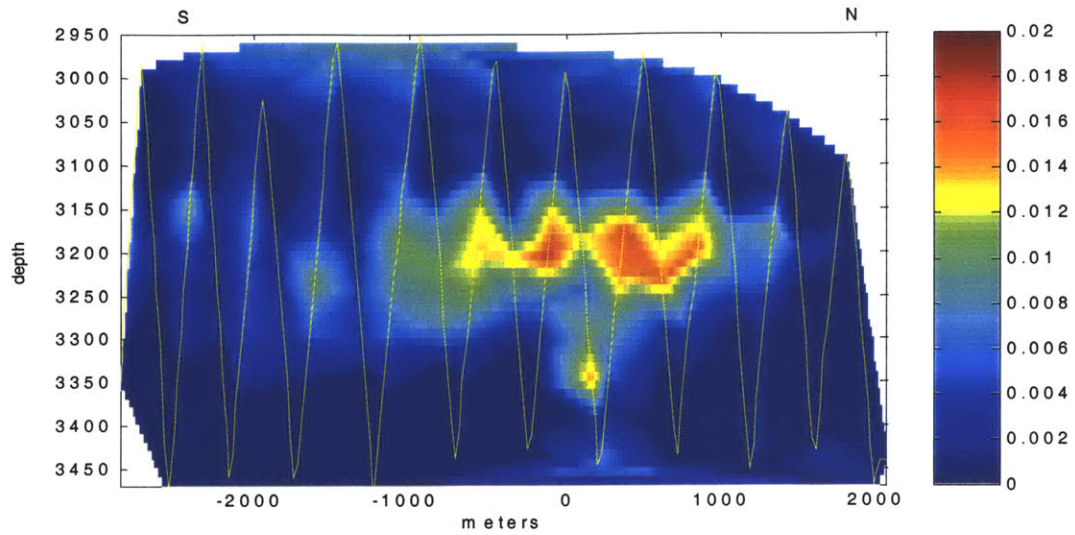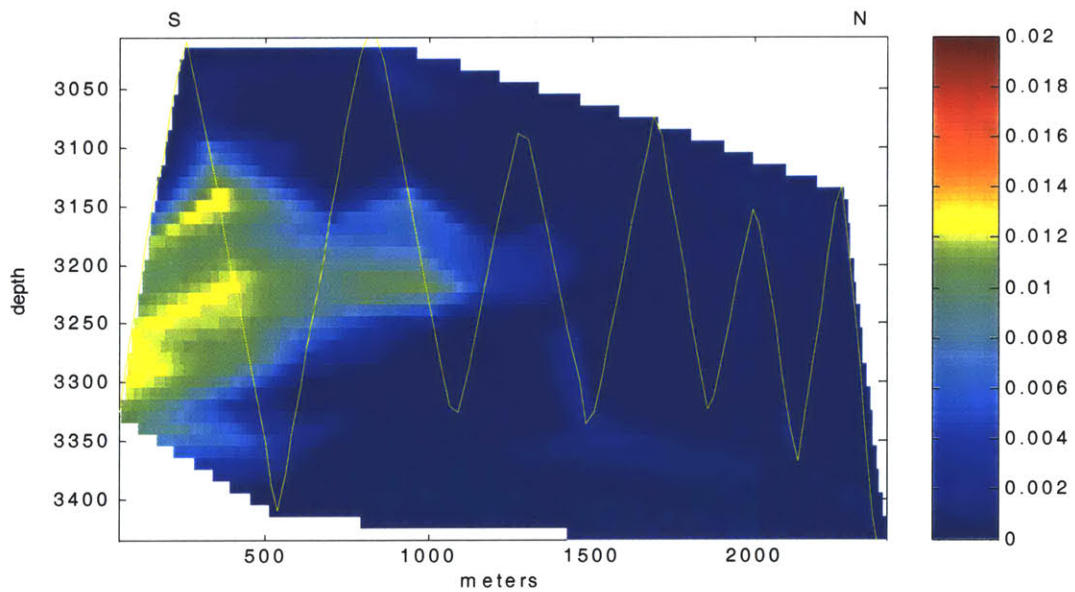
Figure 12: Track axially aligned (2004).

Figure 13: Track back toward the mound (2004).

The first leg depicted in figure 11 took 3 hrs, from 7:00 – 10:00 GMT. On a 12.5 hour
tidal cycle this is at the limit of what one could call a stationary process and the figure

shows the plume in a time averaged sense. The leg shown in figure 12 was taken between 11:30 and 17:00. This 5 hour period is too long to be called stationary, and one must understand that this picture is time aliased. There likely is no more plume activity at the south west corner of the NBL when we are at the northerly boundary. The leg depicted in figure 13 was taken from 18:00 – 20:30 GMT. Interestingly enough we see that the plume has reversed itself in a 12 hr time period, extending roughly 1.5 km north of the central complex. Finally we did a cross axial survey (figure 14) where we started east of the TAG mound and proceeded over the mound in an westerly direction, again perpendicular to the direction of the axial valley.
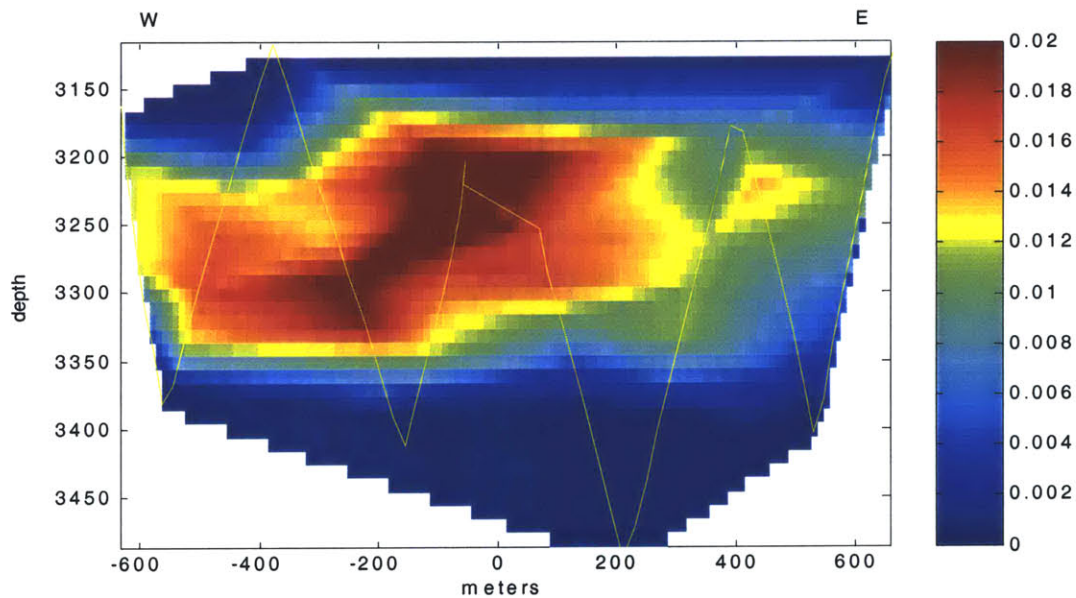
Figure 14: Cross-axial leg (2004).

The cross-axial leg shown in figure 14 reveals that there is hydrothermal water extending 700 meters on either side of the plume. This data set shows that there is a tidal current near the TAG mound that advects the hydrothermal water back and forth in the axial direction of the valley. The plume appears elliptical in shape with a half length of 2 km and a half width of 700 m.

2.4 Velocity measurements in the axial valley

During STAG IV we deployed an 'elevator'; a aluminum frame with glass spheres for buoyancy, on an acoustic release, and an upwards looking ADCP mounted to the frame. See figure 15.
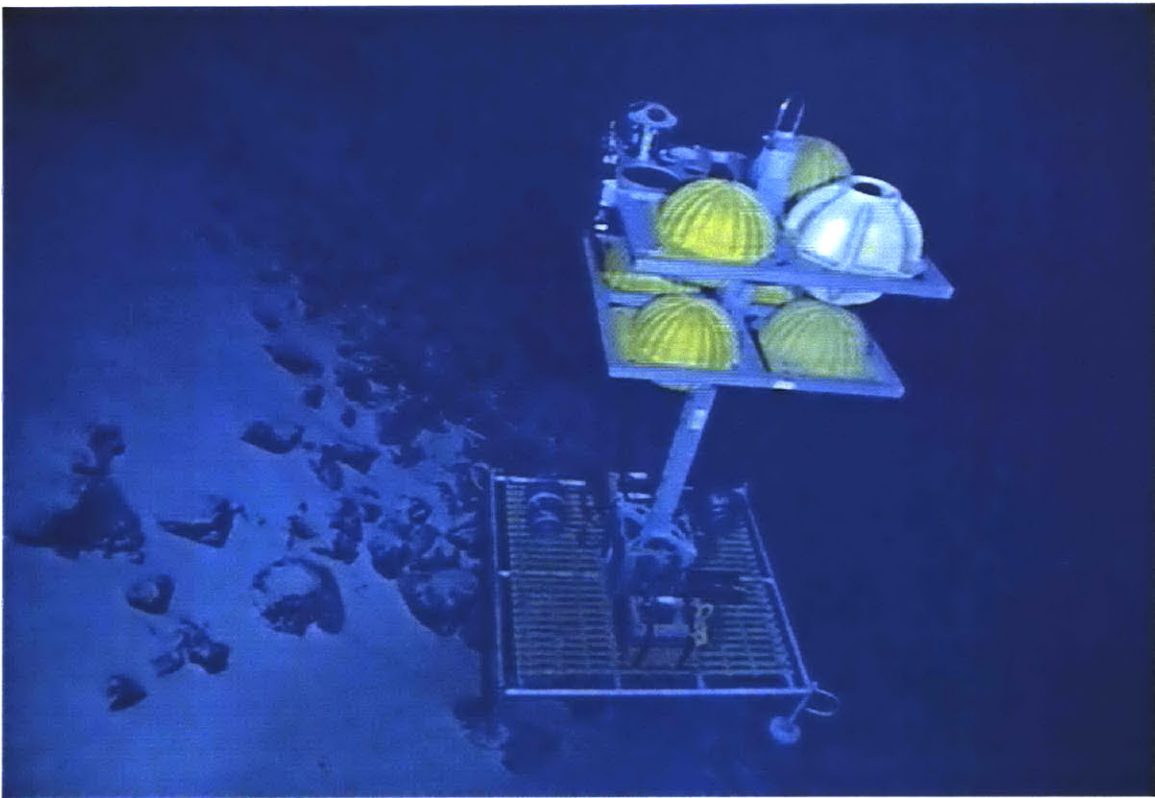
Figure 15: Elevator with ADCP.

The elevator landed on a steep slope at a depth of 3700 meters and balances precariously on the side of a hill. The ADCP is visible in the rear left corner of the elevator. The side of the elevator facing the hill (the left side in figure 15) has a true heading of 90 degrees. The 300 kHz Doppler is expected to have a range of at least 100 meters, but in our data set the maximum range is 50 meters. Perhaps there are very few scatterers in the water. We used sophisticated smoothing routines written by Gene Terray.

We first average the velocities in 5 minute intervals, and second we average the velocities over the entire 50 meter range. Figures 16-18 show the North and East setting velocities during the approximately 50 hours the elevator was on the ocean floor.
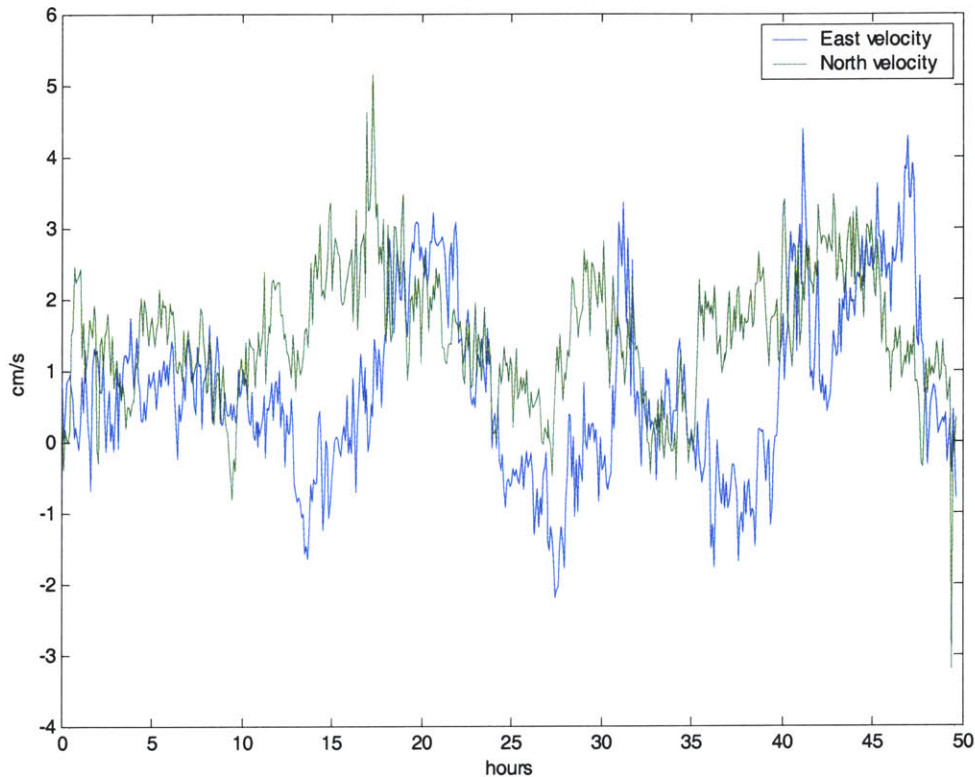
Figure 16: Velocities in the middle of the axial valley.

Low pass filtering the data with a cutoff frequency of 3 cycles per day reveals a tidal signal in the current dataset. Figures 17 and 18 show the velocities again, with the low passed signal superimposed on the raw data. Finally figure 19 shows the power spectrum of both the Norh and East setting velocities. The power spectrum is normalized so that the area under the spectrum curve equals the variance in the signal. The figure does not show the entire spectrum, only the lower frequency bands of interest.
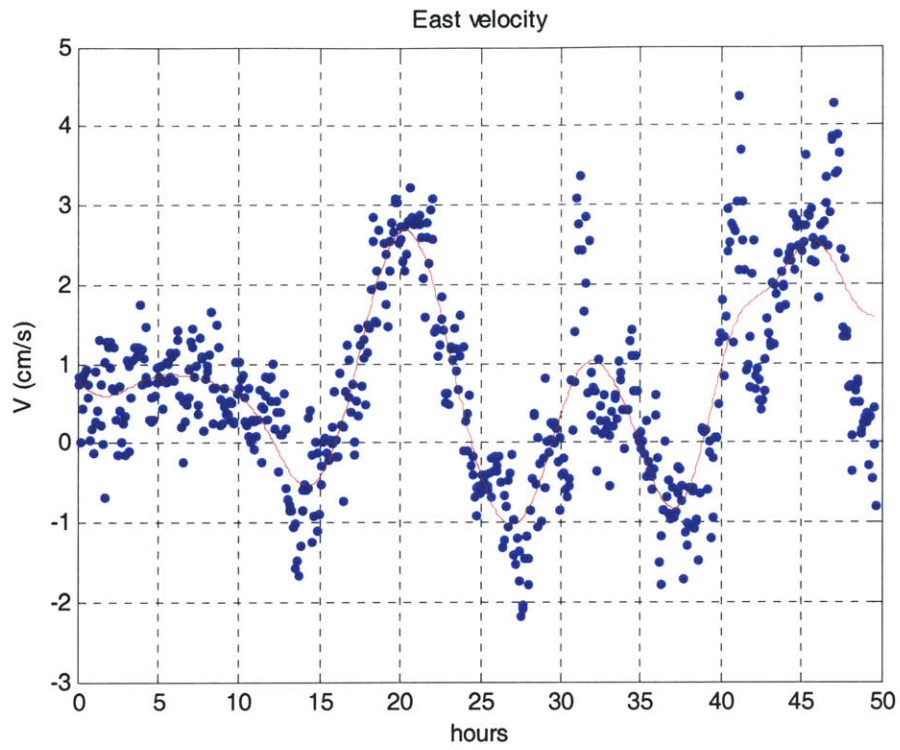
Figure 17: East setting velocity low pass filtered.
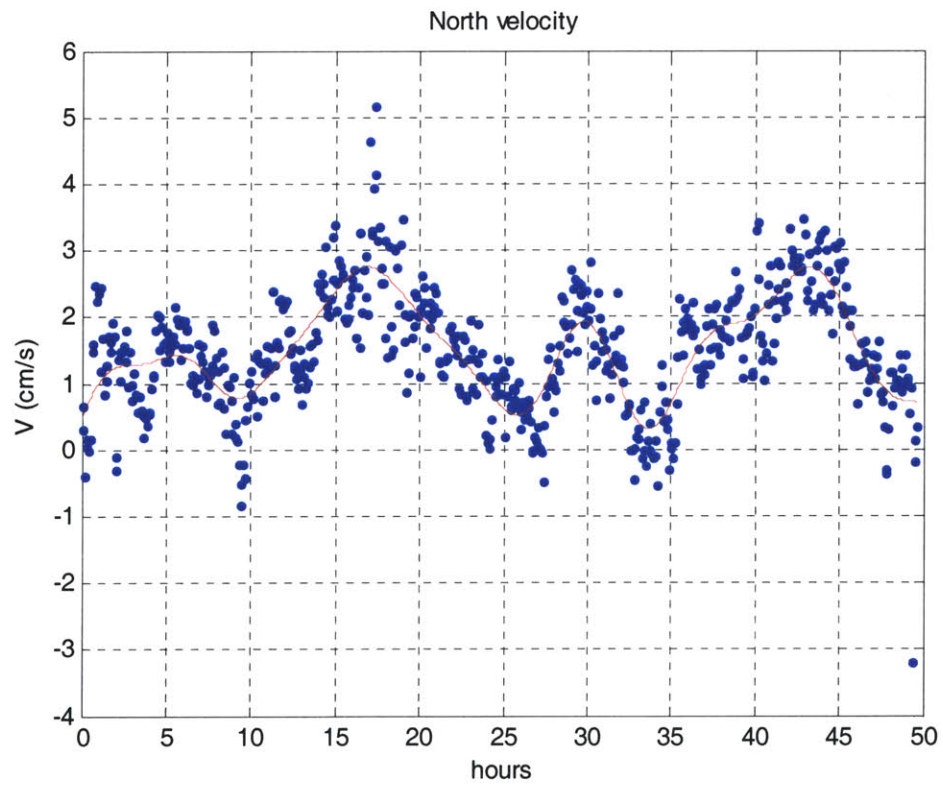
Figure 18: North setting velocity low pass filtered.
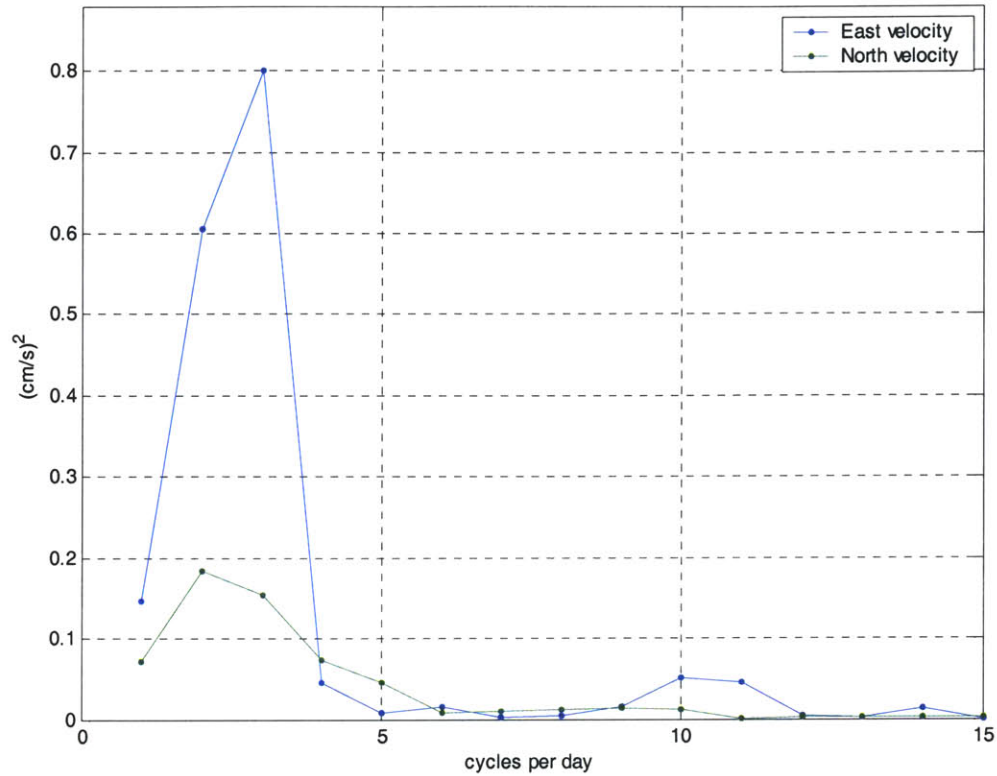
Figure 19: Power spectrum of velocities

The spectral low frequency band is quite wide; it is hard to resolve one unique frequency. Figure 20 shows the rotary spectrum of the lowpassed data. It now becomes apparent that there are two distinct frequencies, and that these low frequency oscillations turn counter clockwise.
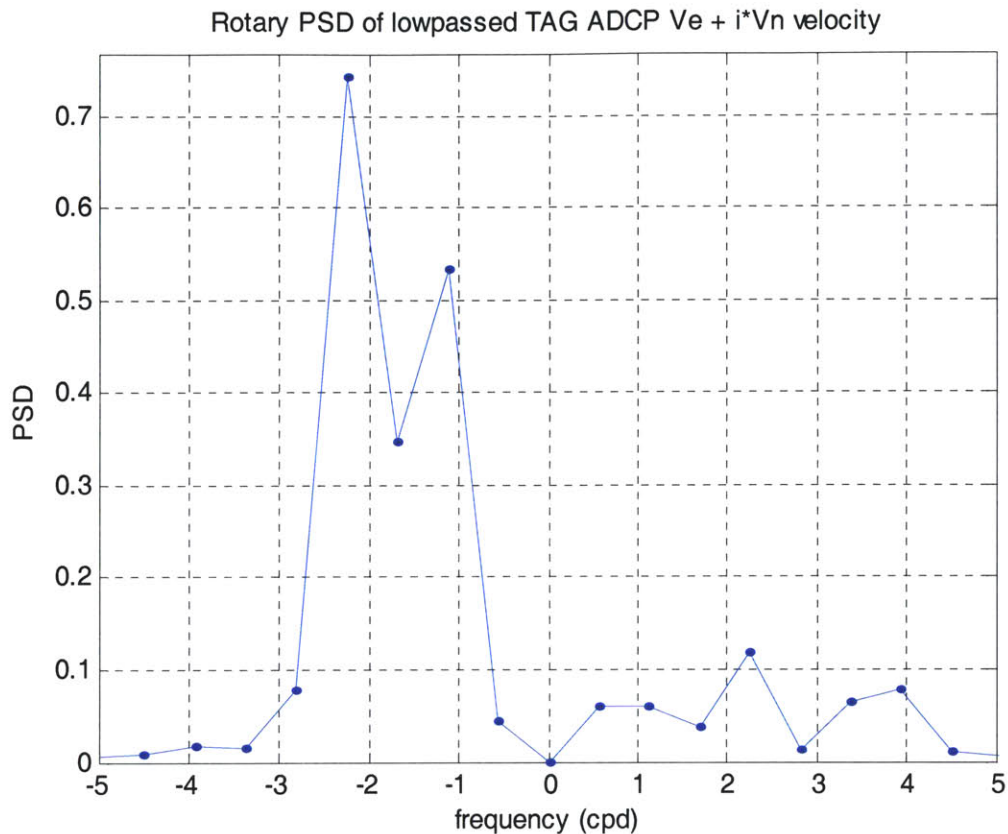
Figure 20: Rotary power spectrum.

Figure 21 shows the scatter plot of East and North setting velocities. There is a clear bias in the current; there is a mean East setting velocity of 0.728 cm/s, and a mean North setting velocity of 1.496 cm/s. That gives us a mean flow with a magnitude of 1.66 cm/s and a direction of 25.9N degrees, which is the direction of the axial valley. Moreover, when we superimpose the lowpassed filtered data on top of the plot we see more indication of two low frequency cycles in the data; one is close to a perfect circle, while the other has a bias towards E-W setting velocities. Figure 22 gives the plot again, but this time the velocities are rotated in valley coordinates.
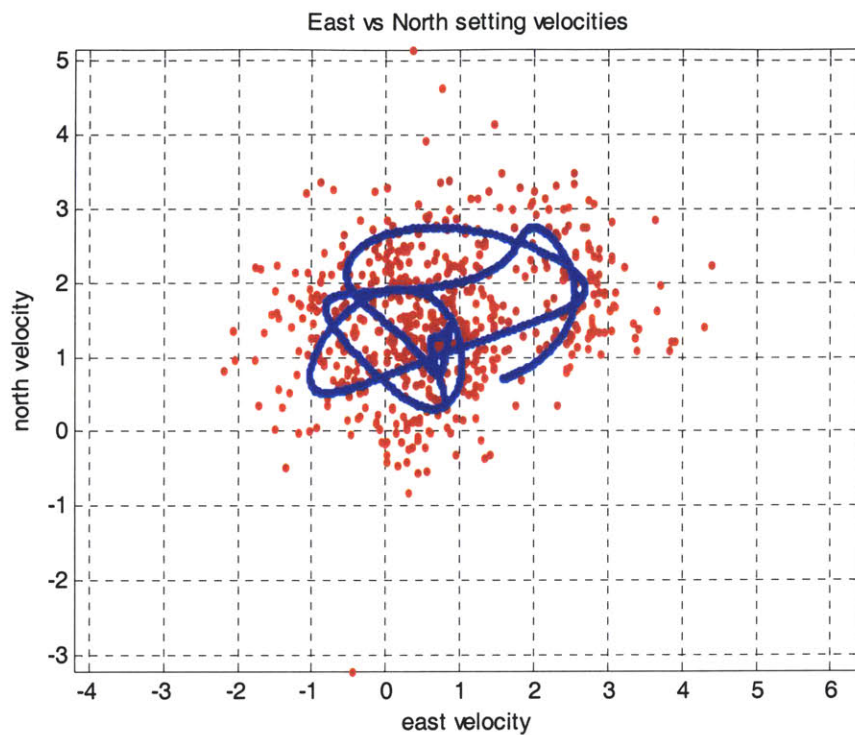
Figure 21: Low passed signal superimposed on the E – N setting velocities.
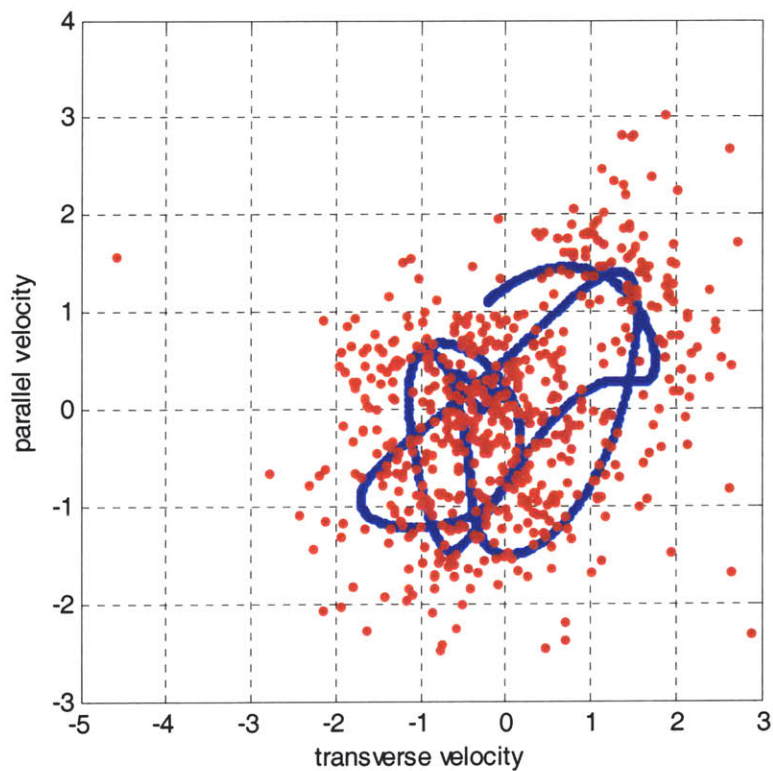
Figure 22: Velocities transformed in axial coordinates.

In summary, there is a mean current setting north-east along the axial valley. This current is of the same magnitude as the tidal currents, which are on the order of 1.5 cm/s. There appear to be two dominant low frequency signals in the data, one which appears to slosh back and forth through the valley (26° N,) and one that appears to have a heading of 19°N.

SECTION 3: MODELING THE BUOYANT PLUME STEM

3.1 Plume models by G.I.Taylor

B.R. Morton, Sir Geoffrey Taylor, and J.S. Turner published a benchmark paper in
1956, using conservation equations to describe plume dynamics. They performed lab
experiments on plumes driven by a buoyancy gradient (as opposed to jets that are driven
by momentum.) (MTT 1955) This model was initially used for atmospheric processes,
and can be used for turbulent plumes. The hydrothermal vent modeling community has
attempted to use this model to describe the plumes found underwater. (Speer and Rona
1989, Rudnicki and Elderfield 1992) The assumptions underlying Taylor's theory are:

- The profiles of vertical velocity and buoyancy force in a plume are similar at all
  heights.
- The rate of entrainment of ambient fluid is proportional to the vertical velocity at
  that height.
- The fluids are incompressible and the change in local densities is small compared
  to a reference density.

3.2 Plume models applied to hydrothermal vents.

Speer and Rona manipulated these conservation equations slightly algebraically, as to
improve their use in numerical solutions:

$$\frac{d(AW)}{dz} = EA^{\frac{1}{2}}W \qquad (1)$$

$$\frac{d(SAW)}{dz} = S_0 EA^{\frac{1}{2}}W \qquad (2)$$

$$\frac{d(TAW)}{dz} = T_0 EA^{\frac{1}{2}}W \qquad (3)$$

$$\frac{d(\rho_i AW^2)}{dz} = g(\rho_0 - \rho)A \qquad (4)$$

Here A is the area, W the vertical velocity, $E = 2\alpha\sqrt{\pi}$ (where α is the entrainment coefficient, experimentally determined by MTT, and taken as .255 by Speer and Rona.) S is salinity, T is the potential temperature, and ρ is the potential density. The subscript 0 indicates background values, whereas no subscript indicates values inside the plume. The subscript i indicates an initial or referenced value – here taken as the density at 3000 meters. The derivation of these equations uses a cylindrical control volume shown in figure 23.
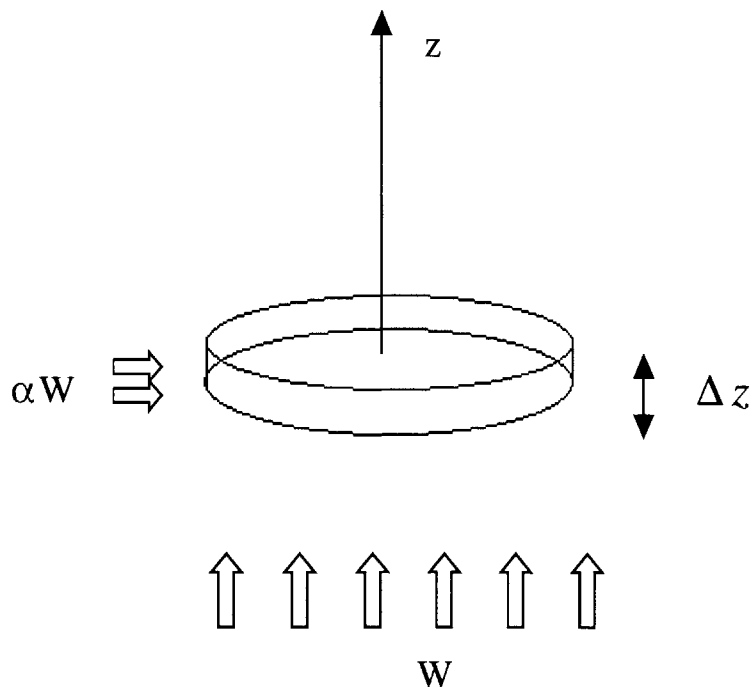

Figure 23: Cylindrical control volume.

Eqn. 1 is obtained by using a Taylor series expansion of the volume flux from the bottom to the top, and equating that to the volume flux through the sides. (Conservation of volume.) If temperature and salinity are conserved, than these scalar quantities simply multiply the volume flux, and we arrive at eqns 2 and 3. Since no momentum is entrained in the plume, only the second order term of the Taylor series remains in the momentum equation (eq 4.) The rate of change of momentum equals the buoyancy force, and the last equation is obtained.

These equations assume a uniform velocity profile, or an average uniform value over any horizontal section, and so the fluxes of mass and momentum are replaced by mean values defined as integrals over the section. (Turner 1973) It is probably more realistic to use the Gaussian velocity profile (McDougall '90), (for the Gaussian velocity profile the right hand side of these equations are multiplied by a factor of 2), but in order to compare the TAG data to the published results we use the uniform velocity distribution in this paper.

We implemented the conservation equations in two different ways: the first algorithm uses an Euler forward differencing scheme outlined in a paper by Rudnicki and Elderfield (Rudnicki 1992), the second algorithm uses matlab's ODE45 solver. With Speer and Rona's initial conditions of $A=.1m^2$, $W=40$ cm/s, $T=300°$, and $S=34.9$ the forward difference algorithm calculates a rise height of 437 m, and matlab's ODE solver gives a rise height of 480m. Figures 24-27 show the profiles of area, salinity, potential temperature, and velocity throughout the plume.
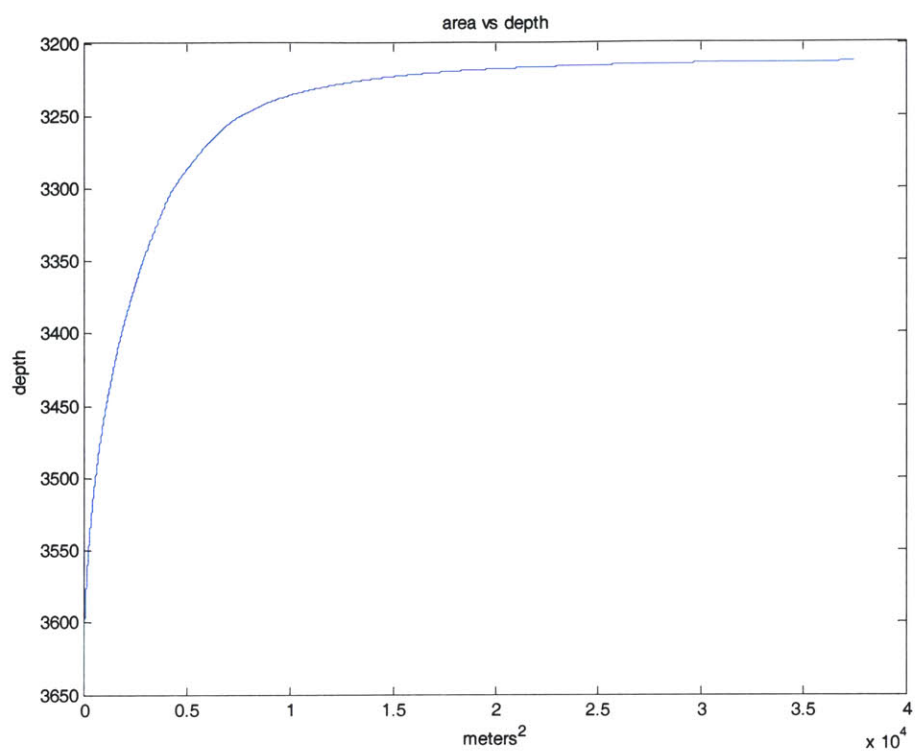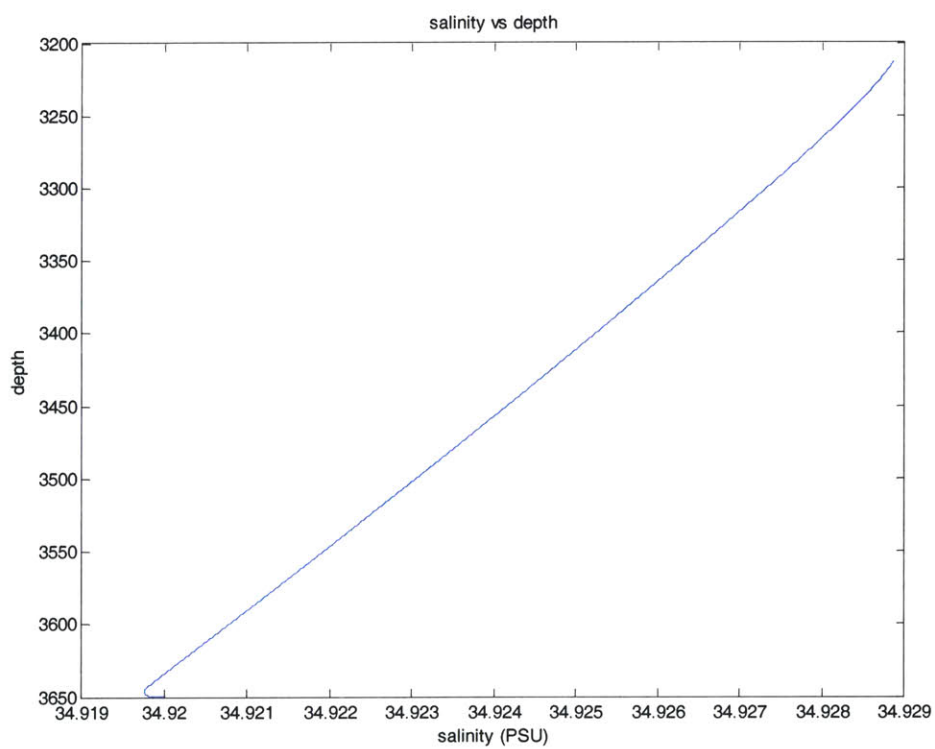
Figure 24: Area of the plume.
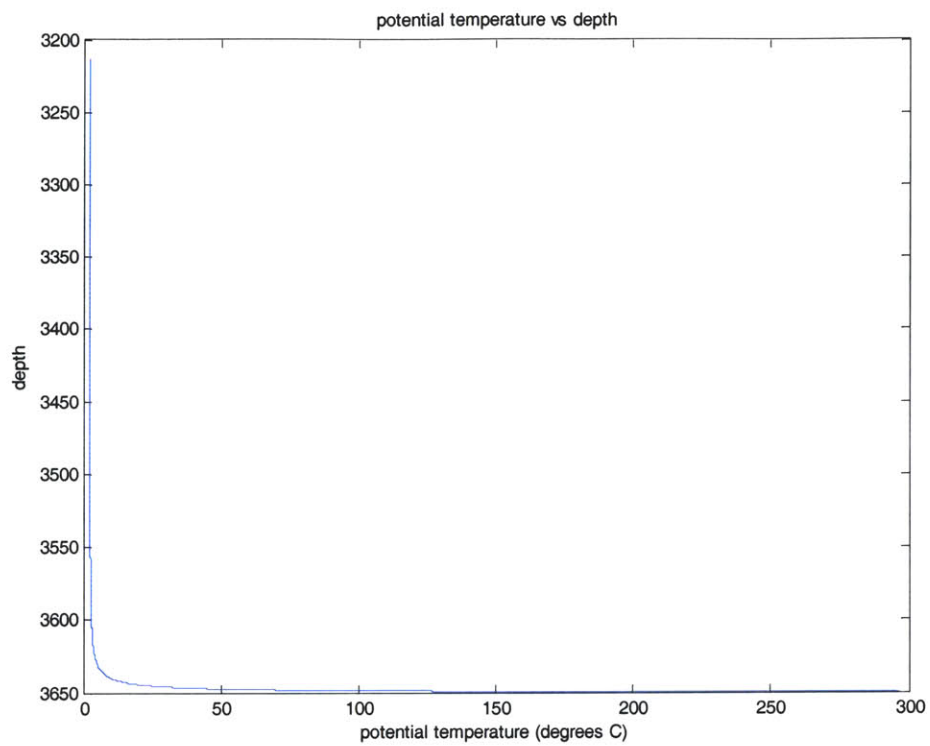

Figure 25: Salinity in plume.
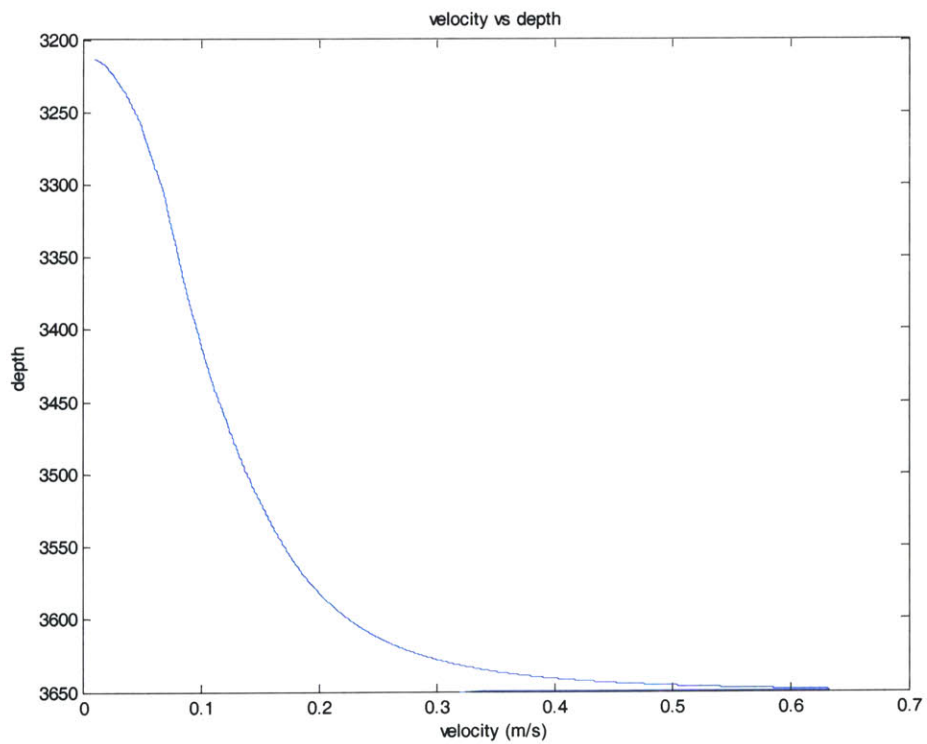
Figure 26: Potential temperature in plume.

Figure 27: Velocity inside plume.

3.3 Empirical methods

The initial conditions used by Speer and Rona are derived from an empirical relationship between plume rise height, density stratification and buoyancy flux. (Turner 1973) For a rising plume in still fluid:

$$z = 5N^{-\frac{3}{4}}B^{\frac{1}{4}} \qquad (5)$$

where z = height of rise of the plume, N is the Brunt-Väisälä frequency, and B is the buoyancy flux.

The Brunt-Väisälä frequency is a measure of the density stratification of the ambient

water, and defined as: $\qquad N = \sqrt{\dfrac{-g * \frac{\partial \rho}{\partial z}}{\rho}} \qquad (6)$

Here ρ is the potential density of the ambient water, taken as 1041.5 kg/m^3. This formula, and all others in this section are calculated from measured values of potential temperature, salinity and pressure according to UNESCO specifications, implemented by Phillip P. Morgan from Australia's CSIRO, in a package of routines called Seawater.

The buoyancy flux is defined as:

$$B = AW\left(\frac{\rho_0 - \rho_i}{\rho_0}\right)g \qquad (7)$$

The subscript 0 indicates background values, and the subscript i indicates a value in the plume. From eqn (5) we find that if the rise height is observed, we can solve for the unknown product of the area and the velocity. This particular AW product, fed into the coupled conservation equations (eqn 1-4), should give the observed rise height. The rise height of TAG for example was observed by Speer and Rona to be approximately 400 meters, and the measured average value of N near the TAG site was calculated at

approximately $9*10^{-4}$ Hz. That gives us a value for the buoyancy flux of about $0.055 \dfrac{m^4}{s^3}$.

Speer and Rona (1989) suggested the following approximation for the equation of state inside the plume:

$$\rho = 1.041548 - \gamma(\Theta - 2.0) + \beta(S - 34.89) \quad (8)$$

where γ is the thermal expansion coefficient, and β the saline contraction coefficient.

$$\begin{aligned} \gamma &= 1.7 * 10^{-4} \\ \beta &= 7.4 * 10^{-4} \end{aligned} \quad (9)$$

The effect of salinity on the density of the exit vent fluid is commonly ignored, and so using Speer and Rona's numbers we estimate the density of the exit fluid to be

$.984 \, g/cm^3$. This is likely a high estimate; Bischoff and Rosenbauer determined

empirically that the density of seawater at 4000 db and 360 °C is $.692 \, g/cm^3$. (Bischoff

1985). Nonetheless, Speer and Rona arrived at the following AW product for TAG:

$$AW = \frac{B}{g(.055)} = .055 \, m^3/s \quad (10)$$

This AW product is slightly higher than the AW product of .04 used in the implementation of the model above.

3.4 Discussion and results.

We can generate an estimate of the heatflux from direct observations of the AW product at TAG. Our best estimate of the exit velocity, W, from dive videos at the TAG mound is 1 m/s. Our best estimate of the main cross-sectional area from SM2000 microbathymetric data acquired during STAG IV (figure 28) is 3 m^2. These values yield an AW product of 3 m^3/s, about two orders of magnitude larger than the Speer and Rona estimate (Speer

and Rona 1989). In order to match the model with initial conditions of this magnitude to our observations we need to increase to entrainment coefficient to ≈ 0.7. Such an increase is conceptually reasonable considering that the empirical value of .255 was derived from tank tests with a single fluid source while at TAG hot fluid vents from several chimneys. These results suggest that care must be taken using eqn (5) to estimate the heat flux from the rise height.
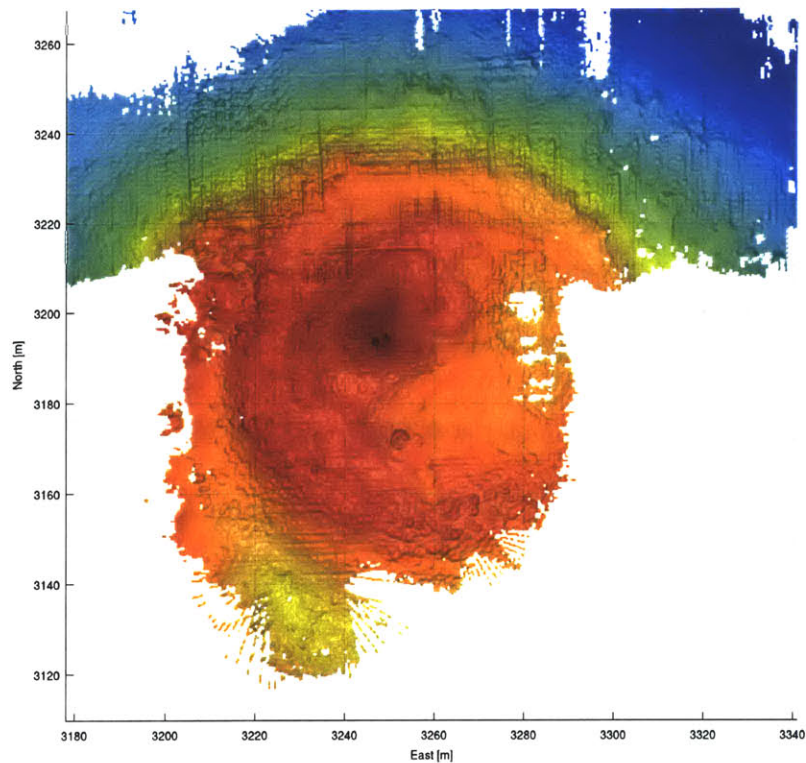
Figure 28: TAG bathymetry. At x = 3246, y = 3193 the two dark features are believed to be chimneys, having a combined area of $\approx 3m^2$.

We can use our numerical model to refine our best estimate of the plume exit velocity. The model accelerates the exit fluids above the initial values unless an initial velocity of 1.3 m/s or greater is used. Forward modeling shows that a velocity of 1.5 m/s predicts the correct rise height of the plume. Plume profiles with these initial conditions are shown if figures 29-31.
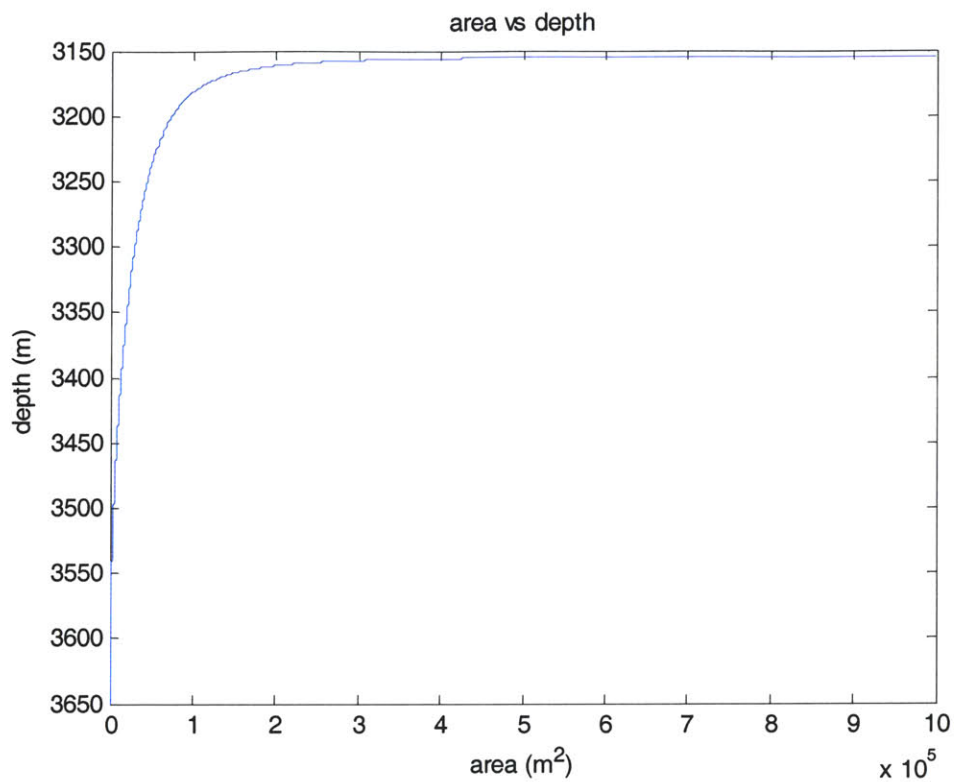
Figure 29: Area of plume stem.
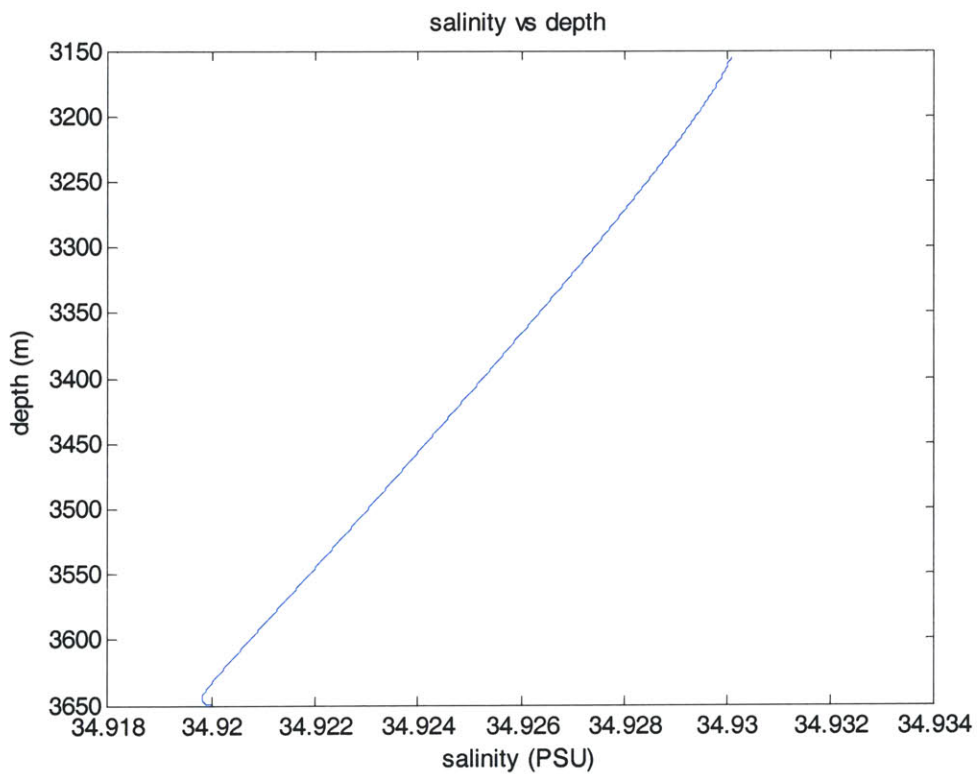
Figure 30: Salinity in plume stem.
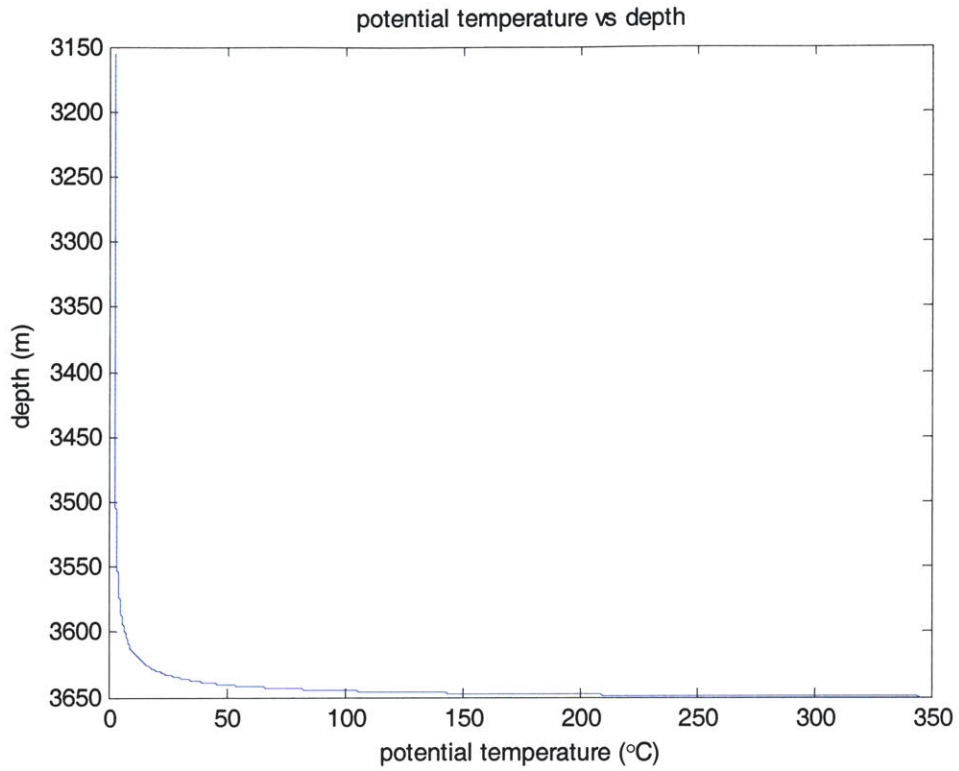
Figure 31: Potential temperature °C in plume stem.
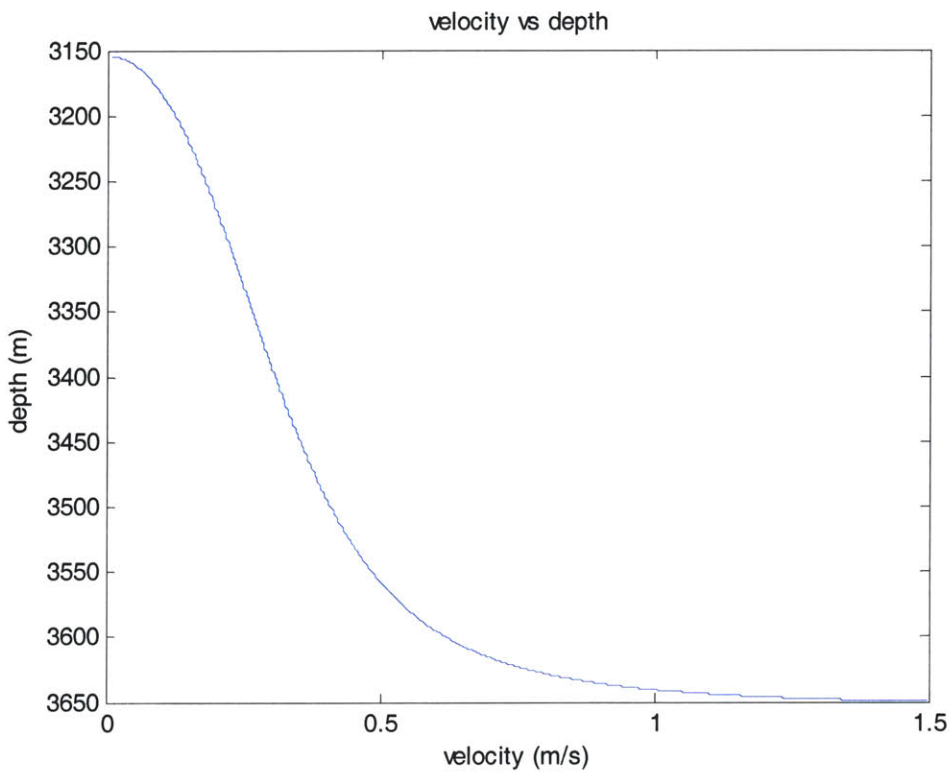
Figure 32: Velocity distribution in plume stem.

3.5 Estimate of TAG heatflux

The canonical heat equation:

$$P = \rho C_p \Delta T A W \qquad (11)$$

Here C_p=6200 $Jg^{-1}{}^{\circ}C^{-1}$ (Bischoff 1985), A=3 m^2, W=1.5 m/s, ρ=692 kg/m^3 (Bischoff 1985), and ΔT=343°C, so:

$$P = 1472e6 * AW = 6624 \text{ MW}.$$

The power output of the vent using an initial AW product of .04 m^3/s – predicted by the empirical relationship using an entrainment coefficient of .255 - would give a power output of 60 MW, underpredicting the power output of the TAG ventfield by 2 orders of magnitude. The heat flux then is given by:

$$H = \frac{P}{A} = \rho C_p \Delta T W = 2208 \frac{MW}{m^2}.$$

SECTION 4: MODELING THE NEUTRALLY BUOYANT LAYER OF THE PLUME.

4.1: Advection diffusion models

At TAG the plume water rises 275 meters before it reaches a level of neutral buoyancy. The neutrally buoyant layer of the plume is 225 meters thick. Since there is no longer a density gradient the convective transport stops, and the plume water is diffused while being advected by the current. Wetzler et all (1998) proposed to use 'puffs' of heat to model this process. The heat output in Joules, Q, during Δt seconds is:

$$Q = P * \Delta t \tag{12}$$

where P is the power supplied by the source (6624 MW). This heat output results in a temperature anomaly ($\Delta\Theta$) of the volume of water (V), with heat capacity Cp and density ρ, directly above the stem, so

$$Q = \rho C_p \Delta\Theta V$$
$$\therefore \rho C_p \Delta\Theta V = P * \Delta t = \rho C_p \Delta T A W \Delta t \tag{13}$$

and

$$V = \left[\frac{\Delta T}{\Delta\Theta} A W \right] \Delta t \tag{14}$$

Since the background temperature in the Atlantic is higher than the temperature in the neutrally buoyant layer we work here again with the temperature anomaly from the temperature salinity plot. This temperature anomaly is not well constrained, and some judgment was used to arrive at an estimated temperature anomaly of .15°C immediately above the plume stem in the neutrally buoyant part of the plume. We then choose a volume that has a length scale on the order of the plume thickness:

$$V = l^3 = 230^3 = 12167 * 10^3 \ m^3.$$

We can now solve for the time step that is required to input this volume:

$$\Delta t = \frac{V}{AW} * \frac{\Delta \Theta}{\Delta T} = 1182 \ s \approx 20 \min.$$

These puffs will now advect with the current, and diffuse at all times. The diffusive process is modeled with the diffusion equation:

$$\frac{\partial \theta}{\partial t} - D \frac{\partial^2 \theta}{\partial t^2} = 0 \qquad (15)$$

This partial differential equation may be solved many different ways, but I will present the solution that makes use of a non dimensional parametrization in the appendix. Further reading on the derivation of the diffusion equation can be found online (Carter 2002). The 3D form of the solution is the product of the three one dimensional solutions:

$$\frac{1}{8}\left\{ erf\left(\frac{x - x_0 + \frac{\Delta x}{2}}{\sqrt{4Dt}} \right) - erf\left(\frac{x - x_0 - \frac{\Delta x}{2}}{\sqrt{4Dt}} \right) \right\} * \left\{ erf\left(\frac{y - y_0 + \frac{\Delta y}{2}}{\sqrt{4Dt}} \right) - erf\left(\frac{y - y_0 - \frac{\Delta y}{2}}{\sqrt{4Dt}} \right) \right\}$$

$$* \left\{ erf\left(\frac{z - z_0 + \frac{\Delta z}{2}}{\sqrt{4Dt}} \right) - erf\left(\frac{z - z_0 - \frac{\Delta z}{2}}{\sqrt{4Dt}} \right) \right\} \qquad (16)$$

where

$$erf(x) = \frac{2}{\sqrt{\pi}} \int_0^x e^{-t^2} dt \qquad (17)$$

The algorithm calculates the position of all puffs in a chosen grid, and the effect at progressive instances of time of all puffs on the grid.

4.2: Discussion and results.

There are few measurements of the current at the Mid Atlantic Ridge (MAR). Murton et all (1999) and Kinoshita (1998) have published MAR velocity profiles near TAG. Thurnherr et all published work undertaken on the MAR in the South Atlantic. Also of interest is the work done at the University of Washington in the East Pacific Rise, particularly the Ph.D. thesis of Scott Veirs (2002). Our velocity measurements do not extend to the level of the NBL, and therefore we can't constrain advection velocities with our data. The ambient velocity, the coefficient of diffusion, the temperature anomaly at the height of the neutrally buoyant layer, and the volume of the puff are all unknown. If we take the coefficient of diffusion as 0.4 m^2/s (Okubo 1971), and if we pick the above numbers for the temperature anomaly and volume, we can illustrate how different flow patterns advect the plume water in different ways. Four different flow patterns are presented. The first one is a constant current of .1 m/s without a tidal surge. The second and third are tidal surges of .1m/s and .01 m/s respectively, and the last one is a tidal surge of .07 m/s with a constant current of .03m/s superimposed on it.

A constant current is shown in figure 33:
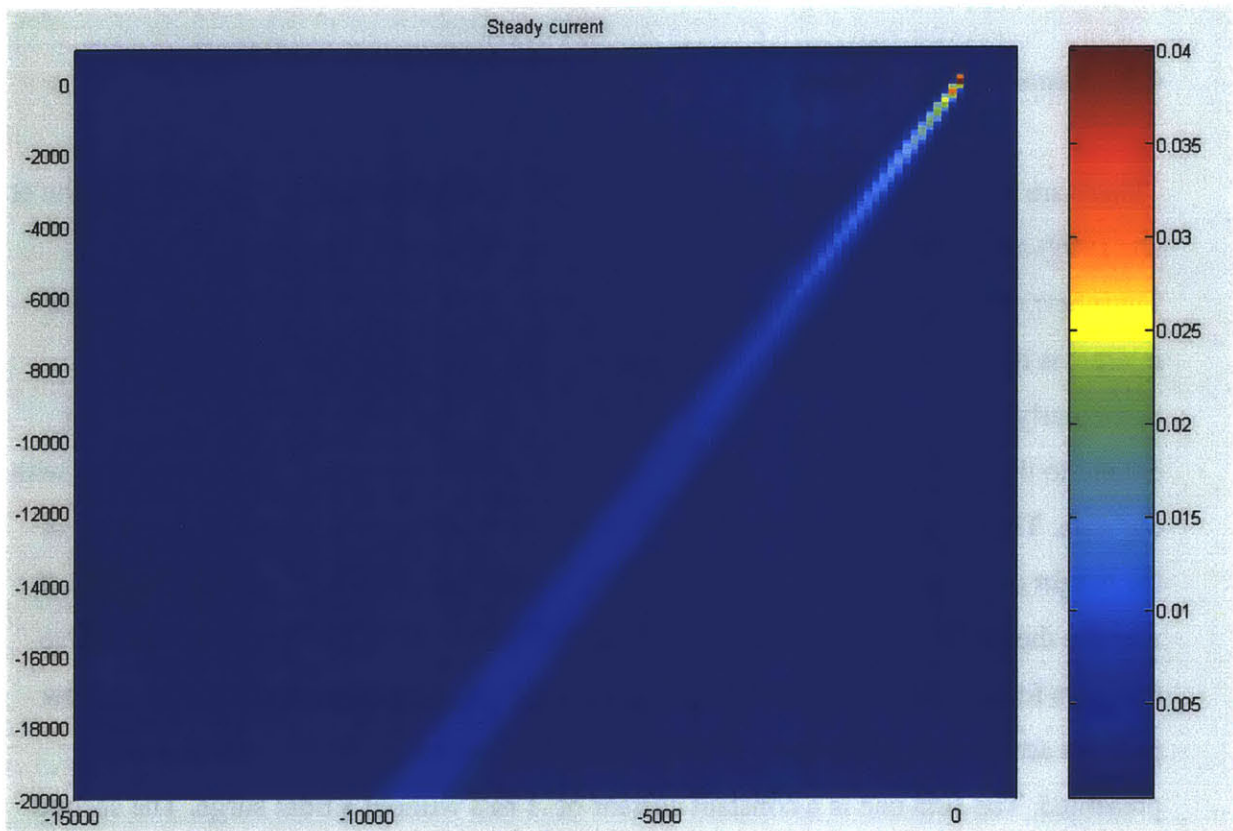
Figure 33: Constant current of .1m/s

Figure 34 shows the flow at slack tide. With the chosen tidal velocity of .1 m/s there is no steady state solution; the warm plume water advects back and forth, leaving no trace of warm water when the tide turns. Note however that there is a warm spot at the end of the tidal excursion caused by the fact that when the tide turns the velocity slows down, allowing warmer water to pool. Figure 35 illustrates that when the tidal velocities are too low, the water will not advect back and forth, but instead will diffuse as if there were no tidal sloshing.
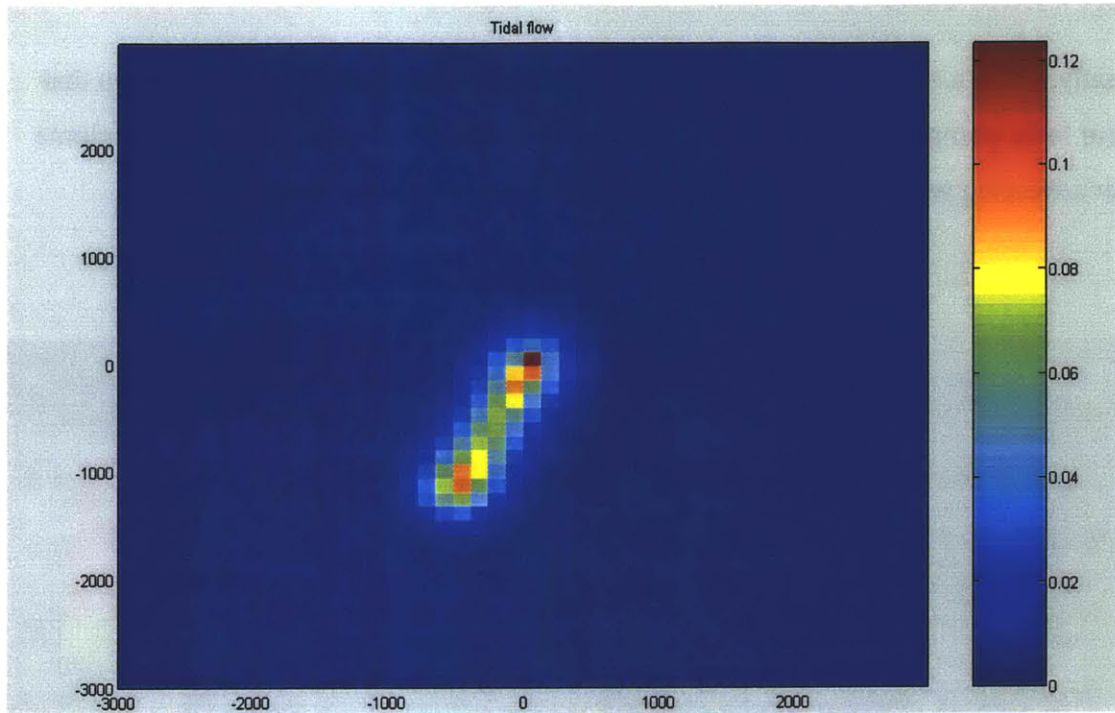
Figure 34: Tidal current of .1m/s
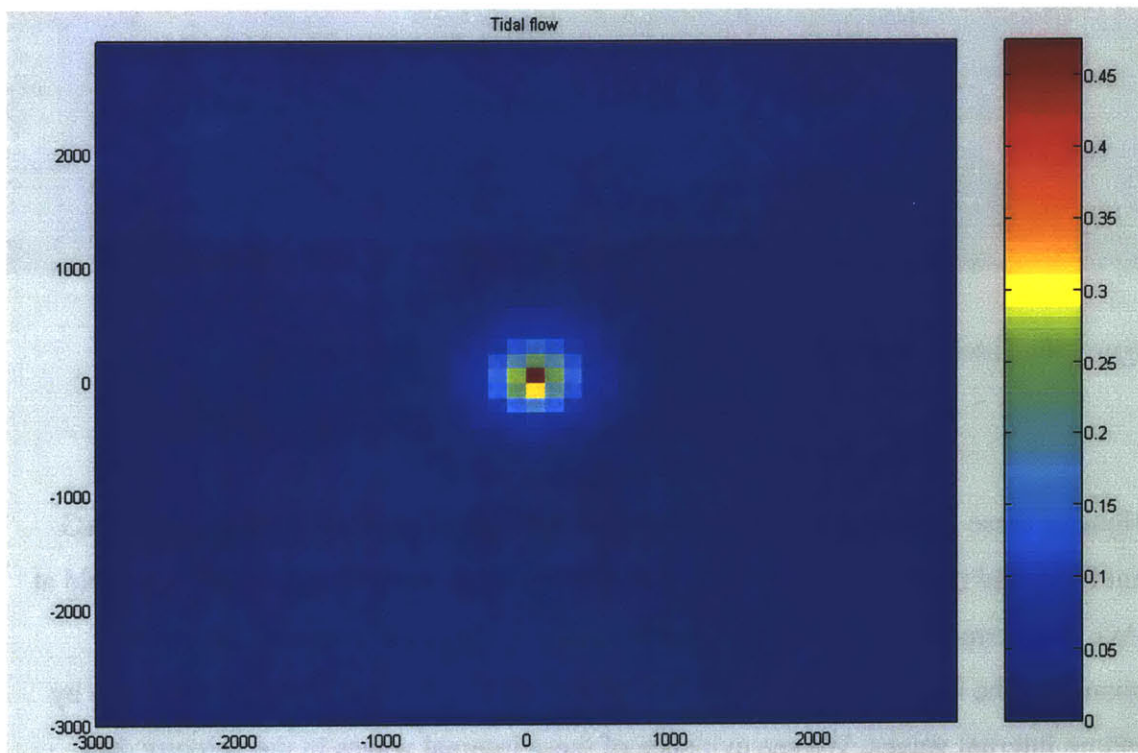
Figure 35: Tidal velocity of .01m/s

Finally, when a mean current is superimposed on the tidal flow, hot spots develop that appear to be pumped in the direction of the current. Figure 36 shows a plot of the plume water advecting with a tidal velocity of .07 m/s and a mean current of .03 m/s.
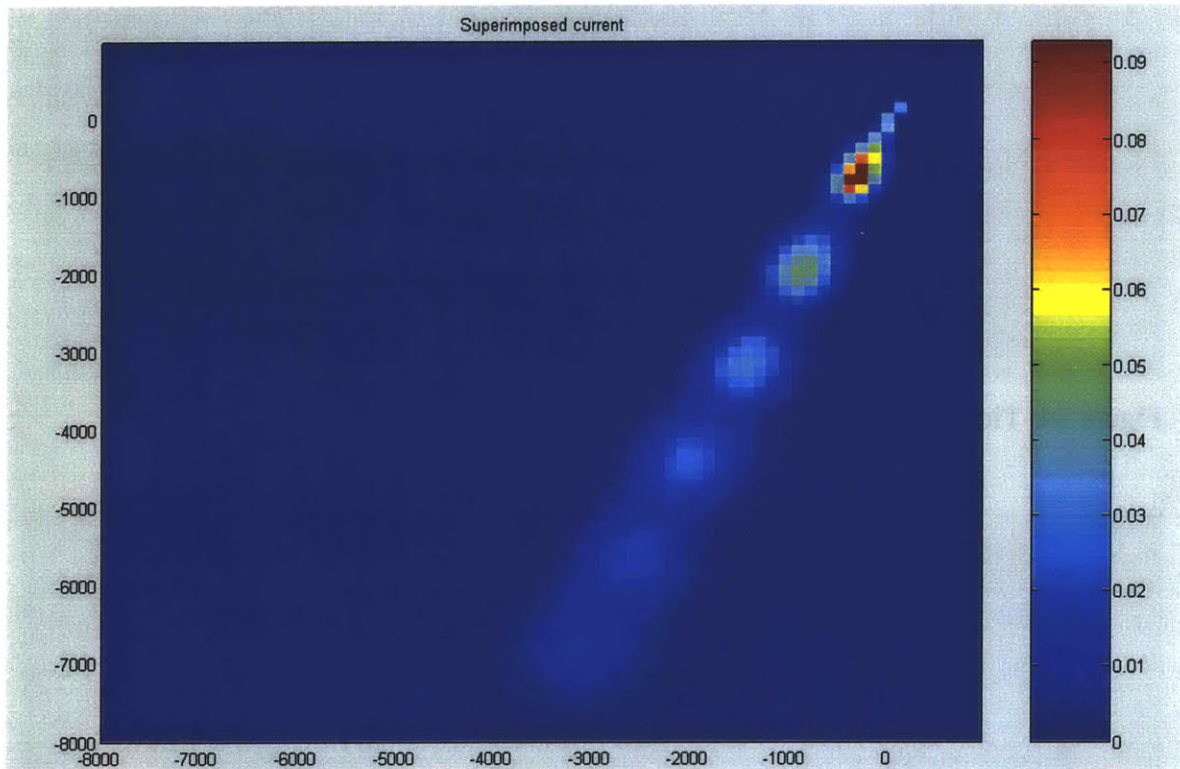
Figure 36: Tidal velocity of .07 m/s superimposed on a .03m/s current.

None of these flow regimes accurately models the observed flow pattern of the TAG vent field, and more velocity measurements are needed constrain the actual flow field at TAG. Furthermore, the model retains too much heat to properly model the plume dynamics. The heat in the neutrally buoyant part of the plume is likely carried away by random internal waves. We see evidence of these internal waves in the velocity data obtained during the ascent and descent of the elevator. Figures 37 and 38 show the east setting velocity during the descent and ascent respectively.
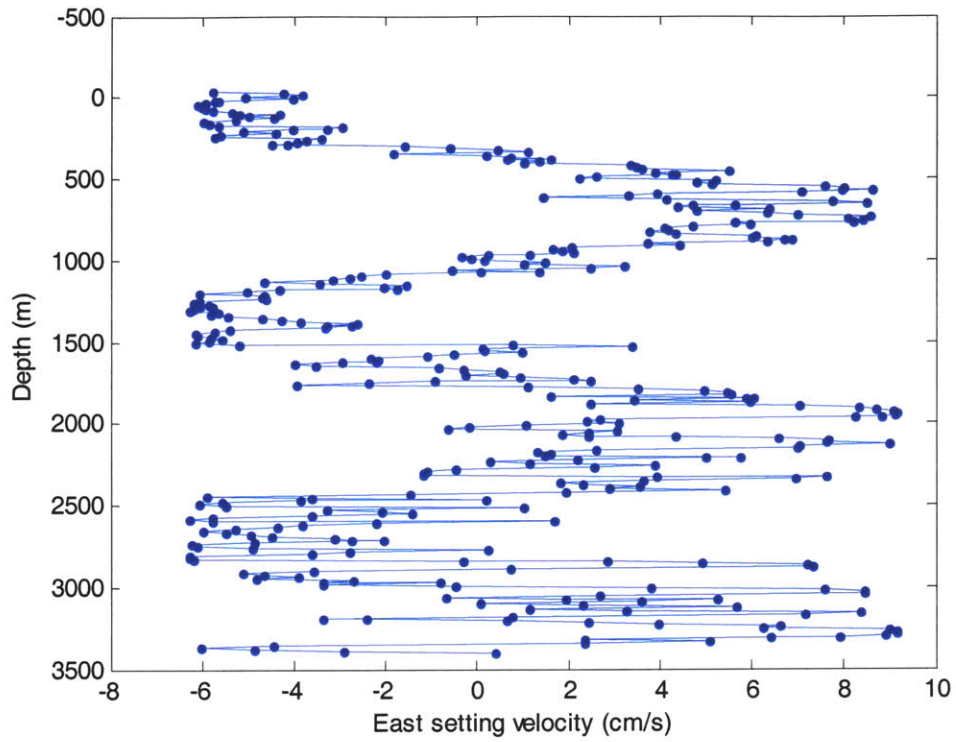
Figure 37: East setting velocity during descent.
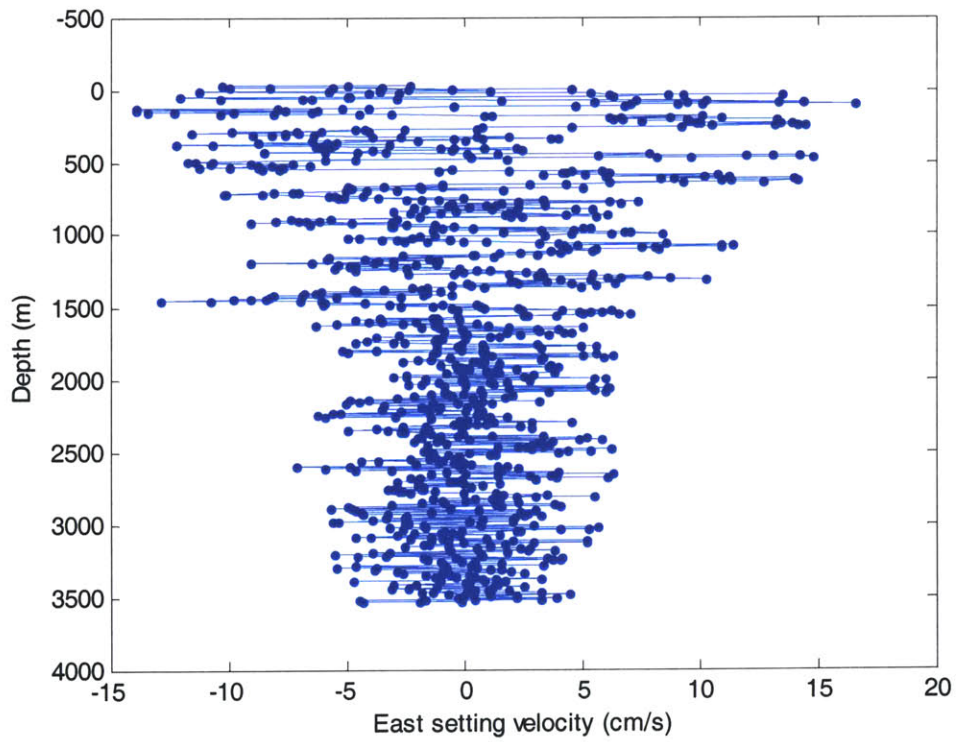
Figure 38: East setting velocity during ascent.

During the descent of the elevator we see a large scale internal wave with a wavelength of almost 1 km. During the ascent of the elevator, two days later at approximately the same time, we see internal waves with a wavelength of at most 100 meters. The ocean generates random velocities that make it impossible to extrapolate currents from the seafloor up to the height of the NBL. The internal waves do dissipate heat from the NBL, and should be incorporated into the model.

SECTION 5: CONCLUSIONS AND FUTURE WORK

My best estimate for the power emitted from the TAG hydrothermal vent field is 6624 MW. This estimate uses the measured area and velocity of the TAG mound. There appears to be considerable more entrainment of ambient fluid into the rising plume stem than was previously assumed. In the first 50 meters off the seafloor there is a mean current setting North in the direction of the axial valley. The velocities have a tidal component, with a period close to 12 hours. The magnitude of the velocities is approximately 1.5 cm/s. It appears as if the plume is advected back and forth by a tidal sloshing in the direction of the axial valley. Velocity measurements are the key to future vent field work. Source velocity measurements could be made with either a MAVs (Modular Acoustic Velocity sensor) or an ADCP. The longest ranging ADCP – the 75 kHz is able to measure velocities up to 1 km away from the instrument - could be moored on the bottom to observe ambient velocities near the plume. This would provide more insight into the dynamic behavior of the neutrally buoyant plume. Plume finding will also be greatly simplified by knowing the ambient currents as the plume water is advected by the ambient currents.

SECTION 6: APPENDIX.

Assume that

$$\theta = \alpha * f(\frac{x}{\sqrt{Dt}})$$

(18)

Normalize the θ distribution to 1:

$$1 = \int dx\theta = \alpha \int_{-\infty}^{\infty} dx f\left(\frac{x}{\sqrt{Dt}}\right)$$

(19)

let

$$\xi = \frac{x}{\sqrt{Dt}}$$

$$d\xi = \frac{1}{\sqrt{Dt}} dx$$

(20)

then

$$\alpha\sqrt{Dt} \int f(\xi)d\xi = 1$$

$$\alpha = \frac{1}{\sqrt{Dt} \int f(\xi)d\xi}$$

(21)

Define

$$\alpha_0 = \alpha\sqrt{Dt}$$

(22)

Then

$$\theta = \frac{\alpha_0}{\sqrt{Dt}} f\left(\frac{x}{\sqrt{Dt}}\right)$$

(23)

$$\frac{d\theta}{dt} = \frac{-\alpha_0}{2t\sqrt{Dt}} f\left(\frac{x}{\sqrt{Dt}}\right) + \frac{\alpha_0}{\sqrt{Dt}} \frac{df}{dt} \frac{-x}{2t\sqrt{Dt}}$$

$$= \frac{-\alpha_0}{2t\sqrt{Dt}} f\left(\frac{x}{\sqrt{Dt}}\right) - \frac{\alpha_0 x}{2tDt} f'\left(\frac{x}{\sqrt{Dt}}\right) \tag{24}$$

$$D\frac{\partial^2\theta}{\partial x^2} = D\frac{\partial}{\partial x}\left[\frac{\alpha_0}{\sqrt{Dt}} f'(\ )\frac{1}{\sqrt{Dt}}\right]$$

$$= \frac{\alpha_0}{t}\frac{\partial}{\partial x} f'\left(\frac{x}{\sqrt{Dt}}\right) = \frac{\alpha_0}{t}\frac{1}{\sqrt{Dt}} f'' \tag{25}$$

Plugging into the diffusion equation:

$$\frac{-\alpha_0}{2t\sqrt{Dt}} f - \frac{\alpha_0}{2t\sqrt{Dt}}\frac{x}{\sqrt{Dt}} f' - \frac{\alpha_0}{t\sqrt{Dt}} f'' = 0 \tag{26}$$

or

$$f + \xi f' + 2f'' = 0 \tag{27}$$

We have reduced the partial differential equation to an ordinary differential equation that may be readily solved:

Let

$$f = e^{-\beta\xi^2}$$

$$f' = -2\beta\xi e^{-\beta\xi^2} \tag{28}$$

$$f'' = -2\beta e^{-\beta\xi^2} + 4\beta^2\xi^2 e^{-\beta\xi^2}$$

So

$$1 - 2\beta\xi^2 - 4\beta + 8\beta^2\xi^2 = 0$$

$$\left(8\beta^2 - 2\beta\right)\xi - 4\beta + 1 = 0 \quad only\ when$$

$$\begin{cases} 8\beta^2 - 2\beta = 0 \\ -4\beta + 1 = 0 \end{cases} \tag{29}$$

$$\Rightarrow \beta = \frac{1}{4}$$

$$\Rightarrow f = e^{-\xi^2/4} = e^{-x/\sqrt{4Dt}}$$

But since

$$\theta = \alpha f\left(\frac{x}{\sqrt{Dt}}\right) \tag{30}$$

and

$$\alpha = \frac{1}{\int f(\xi)d\xi\sqrt{Dt}} = \frac{1}{\sqrt{\pi 4Dt}} \tag{31}$$

so

$$\theta = \frac{1}{\sqrt{\pi 4Dt}} e^{-x^2/4Dt} \tag{32}$$

This is the well known solution to the diffusion equation in one dimension, and it may be shown that it is also the Green function, or the fundamental solution. The puff is modeled as a square pulse in x, y, and z, so the solution in any of the spatial variables should be integrated over the pulse. The solution may then be extended to three dimensions as x y and z are all independent variables, and so the product of the solutions is a valid solution to the three dimensional problem. Figure 37 sketches the coordinate system for the puff; at any time t the origin of the moving puff is located at x_0.
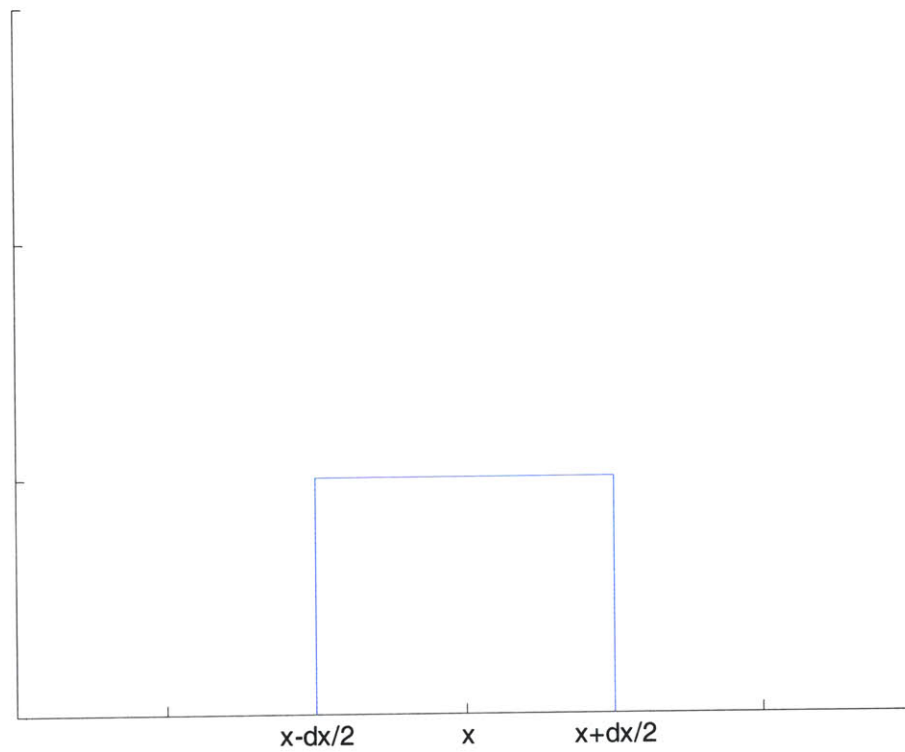
Figure 37: Puff coordinate system.

The integration proceeds as follows:

$$\frac{1}{\sqrt{\pi 4Dt}} \int_{x-x_0-\frac{\Delta x}{2}}^{x-x_0+\frac{\Delta x}{2}} e^{\frac{-x^2}{4Dt}} dx \qquad (33)$$

Let $s = \dfrac{x}{\sqrt{4Dt}}$, and $ds = \dfrac{dx}{\sqrt{4Dt}}$, then

$$\frac{1}{\sqrt{\pi}} \int_{\left(x-x_0-\frac{\Delta x}{2}\right)\Big/\sqrt{4Dt}}^{\left(x-x_0+\frac{\Delta x}{2}\right)\Big/\sqrt{4Dt}} e^{-s^2}\, ds \tag{34}$$

$$= \frac{1}{2}\frac{2}{\sqrt{\pi}}\left[\int_{0}^{\left(x-x_0+\frac{\Delta x}{2}\right)\Big/\sqrt{4Dt}} e^{-s^2}\, ds - \int_{0}^{\left(x-x_0-\frac{\Delta x}{2}\right)\Big/\sqrt{4Dt}} e^{-s^2}\, ds\right] \tag{35}$$

$$= \frac{1}{2}\left\{ erf\left(\frac{x-x_0+\frac{\Delta x}{2}}{\sqrt{4Dt}}\right) - erf\left(\frac{x-x_0-\frac{\Delta x}{2}}{\sqrt{4Dt}}\right) \right\} \tag{36}$$

where

$$erf(x) = \frac{2}{\sqrt{\pi}} \int_{0}^{x} e^{-t^2}\, dt \tag{37}$$

The 3D form of the solution is the product of the three solutions:

$$\frac{1}{8}\left\{ erf\left(\frac{x-x_0+\frac{\Delta x}{2}}{\sqrt{4Dt}}\right) - erf\left(\frac{x-x_0-\frac{\Delta x}{2}}{\sqrt{4Dt}}\right) \right\} * \left\{ erf\left(\frac{y-y_0+\frac{\Delta y}{2}}{\sqrt{4Dt}}\right) - erf\left(\frac{y-y_0-\frac{\Delta y}{2}}{\sqrt{4Dt}}\right) \right\}$$
$$* \left\{ erf\left(\frac{z-z_0+\frac{\Delta z}{2}}{\sqrt{4Dt}}\right) - erf\left(\frac{z-z_0-\frac{\Delta z}{2}}{\sqrt{4Dt}}\right) \right\} \tag{38}$$

SECTION 7: BIBLIOGRAPHY

Alt, J.C., Subseafloor Processes in Mid-Ocean Ridge Hydrothermal Systems. *Seafloor Hydrothermal Systems: Physical, Chemical, Biological, and Geological Interactions*, 85 – 114, 1995.

Baker E. T., German C.R., and Elderfield H., Hydrothermal Plumes over Spreading-Center Axes: Global Distribtions and Geological Inferences. *Seafloor Hydrothermal Systems: Physical, Chemical, Biological, and Geological Interactions*, 47-71, 1995.

Bischoff, J. L., and Rosenbauer, R. J., An empirical equation of state for hydrothermal seawater (3.2 NaCl). *American Journal of Science*, Vol. 285, 725-763, Oct 1995.

Carter, WC, 2002: Lecture notes course 3.21
http://pruffle.mit.edu/~ccarter/3.21/Lecture_07/ (Viewed Jan 1st 2005)

Hannington, M. InterRidge: Hydrothermal Vent Sites http://interridge.org (Viewed Dec 31st 2004)

Humphris, S. E., Zierenberg, R.A., Mullineaux, L.S., and Thomson, R.E., eds. *Seafloor Hydrothermal Systems: physical, chemical, biological, and geological interfactions*. American Geophysical Union, Washington D.C., 1995

Hessler, R.R., and Kaharl, V.A., The Deep-Sea Hydrothermal Vent Community: An Overview. *Seafloor Hydrothermal Systems: Physical, Chemical, Biological, and Geological Interactions*, 72 – 84, 1995.

Kadko, D.C., Rosenberg, N.D., Lupton, J.E., Collier, R.C., and Lilley, M.D., Chemical reaction rates and entrainment within the Endeavour ridge hydrothermal plume, *Earth Planet. Sci. Lett.*, Vol 99, 315-335, 1990.

Kinoshita, M., Von Herzen, R.P., Matsubayashi, O., Fujioka, K., Tidally driven effluent detected by long-term temperature monitoring at the TAG hydrothermal mound, Mid-Atlantic Ridge. *Physics of the Earth and Planetary interiors*, Vol. 108, 143-154., 1998.

Klinkhamer, G., Elderfield, H., Greaves, M. Rona,P., Nelsen, T., Manganese geochemistry near high temperature vents in the Mid-Atlantic Ridge rift valley. *Earth and Planetary Science Letters*, Vol 80, 230-240, 1986.

Lavelle, J.W., and Wetzler, M.A., Diffuse venting and background contributions to chemical anomalies in a neutrally buoyant ocean hydrothermal plume. *Journal of Geophysical Research*, Vol. 104, No. C2, 3201-3209., 1999

Lavelle, J.W. Wetzler, M.A. Baker, E.T. and Embley, R.W., Prospecting for Hydrothermal Vents Using Moored Current and Temperature Data: Axial Volcano on the

Juan de Fuca Ridge, Northeast Pacific. *NOAA/Pacific Marine Environmental Laboratory Contribution Number 2135.*, 2001.

Lupton, J.E., Hydrothermal Plumes: Near and Far Field. *Seafloor Hydrothermal Systems: Physical, Chemical, Biological, and Geological Interactions*, 317-346, 1995.

McDougall, T. J., Bulk properties of "hot smoker" plumes. *Earth and Planetary Science letters*, Vol 99, 185-194, 1990.

McDuff, R.E., Physical Dynamics of Deep-Sea Hydrothermal Plumes, *Seafloor Hydrothermal Systems: Physical, Chemical, Biological, and Geological Interactions*, 357-368, 1995.

Morton, B.R., Taylor, G. F. R. S., and Turner, J.S., Turbulent gravitational convection from maintained and instantaneous sources. *Proc. Roy. Society London*, Series A, 234 1-23, 1956.

Murton, B.J. Redbourn, L.J., German, C.R., Baker, E.T., Sources and fluxes of hydrothermal heat, chemicals and biology within a segment of the Mid-Atlantic Ridge. Earth and Planetary Science Letters, Vol 171, 301-317, 1999.

Okubo, A. Oceanic diffusion diagrams. *Deep-Sea Research*, Vol. 18, 789-802,1971.

Pickard, G.L., and Emery, W.J., *Descriptive Physical Oceanography*, 662pp., Pergamon Press, New York, 1964.

Rudnicki, M.D., and Elderfield, H., Theory applied to the Mid-Atlantic Ridge hydrothermal plumes: the finite-difference approach. *Journal of Volcanology and Geothermal Research 50*, 161-172, 1992.

Speer, K. G., and Rona, P. A., A Model of an Atlantic and Pacific Hydrothermal Plume, *Journal of Geophysical Research.*, Vol. 94, 6213-6220, May 1989.

Tivey, M. K., The Remarkable Diversity of Seafloor Vents, *Oceanus* Vol 42, No2, 60-65, 2004

Turner, J.S. *Buoyancy effects in Fluids*, 367 pp., Cambridge Univ. Press, New York, 1973.

Turnherr, A.M., and Speer, K.G., Boundary Mixing and Topographic Blocking on the Mid-Atlantic Ridge in the South Atlantic. Journal of Physical Oceanography, Vol 33, 848-862, 2002.

Veirs, S.R. Heat flux and hydrgraphy at a submarine volcano: Observations and models of the Main Endeavour vent field in the northeast Pacific.
http://econscience.org/scott/pubs/thesis.pdf (Viewed Jan 2005)

Wetzler, M.A., Lavelle, J.W., Cannon, G.A., and Baker, E.T., Variability of temperature and currents measured near Pipe Organ hydrothermal vent site. *Mar. Geophys. Res.,* 20, 505-516, 1998.

7915. 66